

**Dielectric materials for electrolyte gated transistor applications**

Journal:	<i>Journal of Materials Chemistry C</i>
Manuscript ID	TC-REV-05-2021-002271.R1
Article Type:	Review Article
Date Submitted by the Author:	29-Jun-2021
Complete List of Authors:	Huang, Wei; Northwestern University, Chemistry; University of Electronic Science and Technology of China Chen, Jianhua; Northwestern University Wang, Gang; Northwestern University Yao, Yao; Northwestern University Zhuang, Xinming; Northwestern University Pankow, Robert; Northwestern University, Chemistry Cheng, Yuhua; University of Electronic Science and Technology of China Marks, Tobin; Northwestern University, Chemistry Facchetti, Antonio; Northwestern University; Flexterra Corporation

Review

Dielectric materials for electrolyte gated transistor applications

Wei Huang,^{*a,b} Jianhua Chen,^b Gang Wang,^b Yao Yao,^b Xinming Zhuang,^b Robert M. Pankow,^b Yuhua Cheng,^a Tobin J. Marks,^{*b} Antonio Facchetti,^{*b,c}

Received 00th January 20xx,
Accepted 00th January 20xx

DOI: 10.1039/x0xx00000x

In this review, we summarize recent progress in developing dielectric materials for electrolyte gated transistors (EGTs). Semiconductors for EGTs have been extensively studied and reviewed since they dominate the key transport properties of these types of transistors. However, the electrolyte dielectric component of these devices is equally important since it provides ionic displacement dominating the device capacitance, driving voltage, switching times, and determines how to integrate EGTs in/with other device components. Thus, the development of electrolyte dielectrics not only affects EGT performance but has enabled new features and opened up new possibilities for EGTs. Liquid electrolytes are more suitable for integration at bio-interface and in sensing applications, while solid electrolytes can be printable and are compatible with circuit monolithic integration. Moreover, understanding the mechanism of electrolyte dielectric gating has also accelerated the expansion of emerging electrolyte-based electric double layer transistors (EDLTs) and electrochemical transistors (ECTs). In this review, we first present the structure and operation of EDLTs and ECTs, for the latter particularly those based on organic semiconductors (OECTs), since they are the major uses of these materials. Next, different types of electrolyte dielectric materials will be discussed, driven by relevant applications. We complete this paper with a summary and outlook of this field.

1. Introduction

The development of modern electronics relies on progress in active and passive materials as well as device engineering.¹⁻⁴ New materials, including conductors, semiconductors, dielectrics, and passive combined with novel device concepts not only make integrated circuits (IC) faster, cheaper and smaller, but also breed new applications including next generation of displays, sensors, and human-machine interfaces. Among all the electronic devices, transistors of different structures and mode of operation are among the most important electronic building blocks. For metal-oxide-semiconductor field-effect transistors (MOSFETs), the channel dimension is regarded as the major figure of merit of central processing unit (CPU), which has now reached 5 nm in commercialized products⁵ and ~1 nm in the state of art prototype circuits.⁶ Thin film transistors (TFTs) are used in active matrix circuits driving flat panel displays⁷ and key components of new type of type of sensors.⁸

In the new era of artificial intelligence and internet of things, transistors which enable efficient human-machine interfacing, low power dissipation, and excellent mechanical durability are highly desirable.⁹⁻¹¹ Electrolyte gated transistors (EGTs) are transistors that are gated with electrolytes rather than conventional solid-state gate insulators. Due to the high capacitance of the electrolyte (typically >

1 $\mu\text{F}/\text{cm}^2$), EGTs can be driven at low operating voltages (even lower than 1 V); moreover, since the formation of an electrical double layer (EDL) is not limited to the TFT geometry, the EGT architecture can be widely tuned based on the application's needs, making it particularly suitable for human-machine interfacing, (bio)sensing, and flexible/stretchable circuits.¹²⁻¹⁴ Electrolyte gating effect has been discovered in 1955s by Brattain and Garrett using germanium as the semiconductor.¹⁵ However, the potential advantages of this effect, such as low operating voltages and reduced complexity of integration have only been extensively explored recently in emerging applications, such as electrical/chemical physiological sensors, artificial neural networks, and printed circuits.¹⁶⁻¹⁹

After extensive research efforts, several semiconductors have been integrated into EGTs, including metal oxides (e.g., ZnO, IGZO, WO_3),²⁰⁻²³ organics and carbonaceous (e.g., PEDOT:PSS, rubrene, CNT),²⁴⁻²⁶ and two-dimensional transition metal chalcogenide (e.g., MoS_2).²⁷ Several reviews focused on the EGT's semiconductor component^{28, 29} while others primarily addressed applications and field of use such as in biosensors,^{10, 30-32} printed devices/circuits,^{33, 34} and synaptic electronics.^{35, 36} However, electrolyte materials, as one of the most important EGT components, have not been systematically reviewed.^{17, 37} Thus in this review article, we first introduce the structure and the working principles of EGTs. Next, we summarize different classes of electrolytes, including liquid-based electrolytes, polymer-based electrolytes, and oxide electrolytes. Finally, this paper is concluded with a summary and outlook.

2. Basics of electrolyte materials and electrolyte gated transistors

^a School of Automation Engineering, University of Electronic Science and Technology of China (UESTC), Chengdu, Sichuan, 611731, China

^b Department of Chemistry and the Materials Research Center, Northwestern University, IL, 60208, USA.

^c Flexterra Corporation, 8025 Lamon Avenue, Skokie, IL, 60077, USA.

Review

An electrolyte is an ionic conductor but an electronic insulator. Unlike conventional gate dielectrics for transistor, such as silicon dioxide and hafnium oxide, which are in the solid state, electrolyte dielectric materials for EGTs can either be in the form of liquids, gels, or solids. In this review we classify the electrolytes for EGTs into six different types based on their compositions and physical states, specifically: Type I, aqueous salt electrolytes; Type II, ionic liquid (IL) electrolytes; Type III, polymer electrolytes; Type IV, ion gel electrolytes; Type V, polyelectrolytes; Type VI, oxide electrolytes.

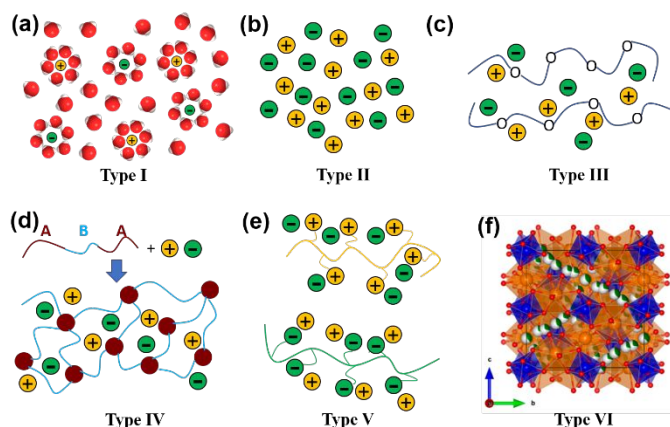


Figure 1. Illustrations of different electrolytes. (a) Type I. Aqueous salt solutions where the first solvation shells of both cations and anions are shown. (b) Type II. Ionic liquids (ILs) consist of pure cations and anions. (c) Type III. Representative polymer electrolytes, where the salt cations and anions are coordinated with polyethylene oxide like polymer chains. (d) Type IV. Representative ion gel electrolytes based on an ABA triblock copolymer and IL, note that the IL is insoluble in the A blocks (maroon) and soluble in the B blocks (blue). (e) Type V. Polyelectrolytes where the upper one based on the polymerization of cations (polycation), while the lower one is based on the polymerization of anions (polyanion). (f) Type VI. A representative oxide electrolyte based on garnet-type cubic $\text{Li}_7\text{La}_3\text{Zr}_2\text{O}_{12}$,³⁸ where the Li atoms are shown as green/white spheres. Reprinted with permission.³⁸ Copyright 2015, American Chemical Society.

Representative chemical structures of these electrolyte families are shown in Figure 1. Among them, Type I and II of electrolytes are in the liquid state. In aqueous salt electrolytes (Type I, Figure 1a), the cations and anions of a salt dissolved in water are typically surrounded by one or several solvation shell(s), also called hydration shell, where the solvent molecules coordinate the ions. Different salt type and concentration lead to different type of solvation shell greatly affecting electrolyte properties. ILs (Type II, Figure 1b) are composed exclusively of cations and anions (Figure 1b). ILs with different chemical structures have been synthesized and play an important role not only in the EGT field but also in other technologies such as batteries, pharmaceuticals, et al.^{37, 39, 40} Three types of electrolytes, Type III-V, contain polymer species in their chemical composition. Polymer electrolytes (Type III, Figure 1c) consist of a polymer or a polymer matrix capable of supporting transport of mobile ions. Typically, the mobile ions are salts, e.g., LiClO_4 , used in aqueous salt electrolytes while the most frequently used polymer is polyethylene oxide (PEO). Ion gels (Type IV, Figure 1d) are composed of a crosslinked polymer network in which an IL is incorporated. Polyelectrolytes (Type V, Figure 1e) are macromolecules that are composed of a single type of charged monomer subunit, and

therefore the overall polymer is either positively or negatively charged. Thus, unlike the previously mentioned electrolytes, where both cation and anions are mobile, in a polyelectrolyte, only cations (in polyanions) or anions (in polycations) are mobile. Finally, oxide electrolytes (Type VI, Figure 1f), are inorganic solids capable of transporting O^{2-} and/or cationic species such as proton (H^+), Li^+ , Na^+ , and other ions. They are widely utilized in batteries and fuel cell^{41, 42} as well as, more recently as gate dielectrics of transistors, especially for artificial synaptic simulations.^{35, 36, 43} A representative oxide electrolyte is based on the garnet-type cubic $\text{Li}_7\text{La}_3\text{Zr}_2\text{O}_{12}$ structure which conducts Li ions.³⁸ In section 3, we will report the details of each electrolyte family along with their representative applications based on their basic properties.

2.1. Key parameters of electrolyte gate dielectrics

A parallel-plate metal-insulator-metal (MIM) device, where the dielectric is sandwiched in between two metal pads (Figure 2a), are typically adopted to characterize the dielectric properties of materials. When a voltage bias (V) is applied between the two electrodes, the dielectric polarizes due to the establishment of an electric field, which induces a net positive charge ($+Q$) at the interface with one electrode and a net negative charge ($-Q$) at that of the other electrode. The amount of charge Q stored in a capacitor is proportional to V according to eq. (1)

$$C = Q/V = \epsilon_r \epsilon_0 A/d \quad (1)$$

where C is the capacitance of the parallel-plate MIM capacitor with an electrode area of A , ϵ_r is the relative permittivity (or typically called dielectric constant), ϵ_0 is the vacuum permittivity, and d is the thickness of the dielectric film. The capacitance per unit area (C_i), which is defined by eq. (2) is a more frequently used parameter of a dielectric.

$$C_i = \epsilon_r \epsilon_0 / d \quad (2)$$

These is no electrical current flowing in an ideal dielectric under any voltage bias until breakdown, however in reality, there is a certain amount of current, defined as leakage current (I_{leak} , or leakage current density, J_{leak}), flowing through the dielectric when a voltage bias is applied. Note, an exponential increase of J_{leak} occurs when a large enough voltage bias (or electric field, $E = V/d$) is applied, due to a portion of the dielectric becoming electrically conductive. This voltage/electric field is called the breakdown voltage (V_b) / breakdown electric field (E_b). C_i , J_{leak} , and V_b are among the most important parameters of a dielectric material when used in a transistor device, as they directly affect the device driving voltage, power dissipation and robustness of operation, and they are typically quantified by carrying out charge transport and impedance spectroscopy measurements. In order to increase C_i , high ϵ_r dielectric materials and thinner dielectrics should be used and, for thin-film transistors, this typically refers to materials with a ϵ_r greater than that of amorphous SiO_2 ($\epsilon_r = 3.6$), preferably that of amorphous Al_2O_3 ($\epsilon_r = 9.1$), and a thickness < 300 nm and preferably < 100 nm for SiO_2 . Typically, a good dielectric for TFTs has a $J_{\text{leak}} < 1 \times 10^{-6}$ A/cm² at 2

MV/cm although lower numbers may be required depending on the device in which the TFT is utilized.⁴⁴

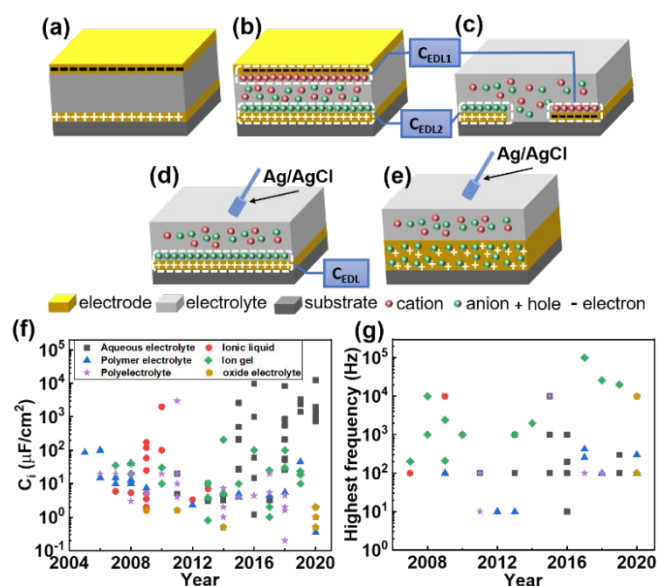


Figure 2. Structures of parallel-plate metal-insulator-metal (MIM) capacitors based on (a) conventional dielectric, and (b) electrolyte dielectric. Schematic diagrams of (c) a planar electrode-based electrolyte capacitor, (d) capacitor with an Ag/AgCl electrode, and (e) capacitor with electrochemically active electrode. Representative capacitances per unit area (f) and highest operable frequencies (g) of different types of electrolytes dielectrics used in EGTs.

Specifically for electrolyte gate dielectrics, C_i , J_{leak} and V_b remain important performance parameters and they can be measured using similar MIM capacitor structures (Figure 2b). However, the electrodes used in these devices are not limited to metals but can involve redox-active materials and semiconductors, thus, the capacitance of electrolyte-based capacitors also depends on the electrode materials (*vide infra*). When a voltage bias is applied, the electrolyte polarizes by the migration of ions leading to the formation of two electrical double layers (EDLs) at both sides of the electrode/electrolyte interfaces of the capacitor. The EDL, which consists of ions at the interfaces screening the opposite charges in the electrode, can be regarded as nanometer-thick capacitors, and the EDL capacitance per unit area can be expressed by eq. (3),

$$C_{\text{EDL}} = \epsilon_r \epsilon_0 / \lambda \quad (3)$$

where ϵ_r is the relative permittivity of the EDL and λ is EDL thickness. ϵ_r and λ are different for different electrolytes, but they are typically >1 and ~ 1 nm, respectively. As a result, C_{EDL} is typically $> 1 \mu\text{F}/\text{cm}^2$.^{45, 46} Consequently, C_i of an electrolyte-based MIM capacitor is expressed as two capacitors in series (eq. 4),

$$C_i = 1 / (1/C_{\text{EDL1}} + 1/C_{\text{EDL2}}) \quad (4)$$

where C_{EDL1} and C_{EDL2} are two EDL capacitances on either side of the electrodes (Figure 2b).

It is worth noting that since the formation of an EDL is not limited to a given capacitor geometry, using a parallel-plate MIM structure

is not essential to extract the capacitance of an electrolyte-based dielectric. Thus, since the construction of a parallel-plate MIM structure is relatively complicated especially for liquid electrolytes, a planar structure (Figure 2c) or replacing one electrode film with a non-polarizable electrode, e.g. Ag/AgCl electrode, (Figure 2d) are also adopted to measure the electrolyte capacitance. Note in a capacitor structure comprising a non-polarizable electrode as in Figure 2d, a negligible voltage drop exists at the non-polarizable side of the capacitor since the capacitance at this side can be regarded as infinitely large, thus, $C_i = C_{\text{EDL}}$. On the other hand, electrochemically-active or porous electrodes could lead to the generation of a bulk EDL/doping in the electrode as shown in Figure 2e. In this case, the charge is stored primarily in the bulk of the electrode and a more common descriptor of the charge storage capacity of the capacitor is the capacitance per unit volume (C^*),⁴⁷ which is given by eq (5)

$$C^* = C_i / d_e \quad (5)$$

where d_e is the thickness of the electrode.

Figure 2f reports representative C_i values of different types of electrolytes based on a survey of the literature. It is obvious that most of the highest C_i values reported to date ($> 100 \mu\text{F}/\text{cm}^2$) are based on Type I aqueous electrolytes. This is mostly due to research highlights for electrochemical transistors (ECT, *vide infra*), where electrochemically active semiconductors have been employed as one of the electrodes of the capacitor (Figure 2e), leading to bulk charge accumulation and, thus, ultra-high C_i values. Except for the high C_i values due to the utilization of electrochemically active electrodes, the other C_i s are within the range of $1 \sim 100 \mu\text{F}/\text{cm}^2$, which are dominated by the formation of the EDL. As mentioned above, C_{EDL} depends on not only the ions of the electrolyte, but also on the electrode material. Ions with small solvated ionic radius are likely to accumulate more efficiently at the interface with the electrode leading to higher C_{EDL} ,⁴⁸ while electrodes that are more hydrophilic would also likely accumulate more charges.⁴⁹ Note that oxide electrolytes typically exhibit lower C_i due to the relatively low ion concentration and the rigid oxide matrix at the interface with the electrode would reduce the active area of the EDL.

Interestingly, in most of the EGT literature, reporting and accurate access of the electrolyte J_{leak} is missing, likely because the leakage current is low as long as the operating voltage is within the highest voltage that the electrolyte can endure. Note J_{leak} of electrolytes can also be accessed from the EGT off-current (I_{OFF}) together with the channel dimensions, and has been reported to be in the range of $10^{-7} - 10^{-4} \text{ A}/\text{cm}^2$, which is typically higher than that of conventional solid-state dielectrics.³³ This also implies a major difference between conventional dielectrics and electrolyte dielectrics, where E_b (or V_b) is typically used to determine the electronic robustness of the conventional gate dielectrics under an electric field and V_b can be effectively increased by simply increasing the thickness of dielectric. However, V_b for electrolyte dielectrics is typically independent of the film thickness/geometry, but it depends

Review

on the electrochemical potential window of the electrolyte. The typical highest voltages that can be applied to electrolytes are lower than 3 V (for aqueous electrolyte, the voltage is typically lower than 1 V; for oxide electrolyte, higher voltages of more than 5 V have been reported.⁵⁰) to avoid the decomposition/side reactions of the electrolytes.⁵¹

The formation of the EDL relies on the drift of mobile ions in the electrolyte under a voltage, thus higher ionic conductivity leads to a faster EDL formation and enables the electrolyte to work at higher operating frequencies. Obviously, compared to conventional dielectric materials, such as SiO₂, the EDL formation time is much longer than that of electronic and orientational polarizations.⁴⁴ Moreover, the polarization time (τ) of an electrolyte depends both on the ionic conductivity (σ), thickness of electrolyte dielectric (d) and C_{EDL} , and it is given by eq (6),³³

$$\tau = RC_{EDL} = dC_{EDL}/\sigma \quad (6)$$

where R is the ion resistance of the electrolyte. Since σ and d_e of an electrolyte are typically $10^{-7} \sim 10^{-1}$ S/cm and $> 0.1 \mu\text{m}$, respectively, the shortest τ is in the range of $\sim 10^{-7}$ s. Consequently, the highest polarization frequencies for electrolyte-based electronic devices are in the MHz range, indicating that EGT-based circuits can be used only for bio-signal monitoring, very slow switching sensors and displays, where the operation frequencies of no greater than 10^7 Hz are required.^{20, 52-54} Based on literature reports, the highest reported frequencies of different types of electrolytes in EGTs are summarized in Figure 2g. It is obvious that the highest operatable frequency of ion gel electrolyte increased steady in the past decade and now approaches 100 kHz,^{21, 55, 56} while for polymer electrolytes and polyelectrolytes, the reported frequencies are typically < 10 kHz.^{57, 58} Compared to other types of electrolytes, ion gels show high ion conductivity ($10^{-5} \sim 10^{-2}$ S/cm; while for polymer electrolytes and polyelectrolyte, it is only $10^{-7} \sim 10^{-4}$ S/cm). Moreover, the thickness and geometry of ion gels can be well controlled compared to aqueous electrolytes and ILs. Consequently, short τ values are more easily accessible for ion gel electrolytes than other electrolytes.

Another important parameter of an electrolyte is the working temperature. Aqueous salt electrolytes show the narrowest working temperature dominated by the freezing and boiling point of the liquid solution. Similarly, the working temperature of ILs is also limited by their melting temperature, which are typically around -20 °C, while the boiling point is less of a concern since it is typically > 400 °C.³⁹ For polymer electrolytes, σ is highly temperature dependent and it increases with the temperature. Thus, typical working temperatures for polymer electrolytes are at room temperature or higher, as long as the high temperature would not start to decompose the electrolyte.⁵⁹ For ion gels, the working temperature is mostly dominated by the IL component and by the decomposition temperature of the polymer. The working temperature of several polyelectrolytes are less studied but they should be similar to that of polymer electrolytes and ion gels. Oxide electrolytes possess the widest working temperature range due to

their thermally stable structure. Temperature as high as 700 °C can be used for some oxide electrolytes.⁶⁰ Consequently, oxide electrolyte can be utilized in applications where high operating temperatures are required.

2.2. Structures and working modes of electrolyte gated transistors

In this review we primarily focus on electrolyte gated transistors which structure can be similar to that of TFTs. These devices comprise of three key essential materials components, the conductor, the dielectric, and the semiconductor functioning as the source/drain/gate electrical contacts, the gate electronic charge insulator, and the charge carrying channel, respectively. There are typically four TFT architectures depending on the relative arrangement of the electrical contacts and the other components (Figure 3a-d), including bottom gate top contact (BGTC), bottom gate bottom contact (BGBC), top gate top contact (TGTC) and top gate bottom contact (TGBC) architectures. However, the most commonly used architectures are the BGTC and TGBC ones since they typically show better transistor characteristics due to superior charge injection characteristics and, for TGBC, facile reduction of the channel length geometry.⁶¹ The most commonly used TFT materials are metals as conductors, undoped silicon, organics and metal oxides as semiconductors, and metal oxides and organic insulating polymers, mainly polyacrylates, as gate dielectrics.

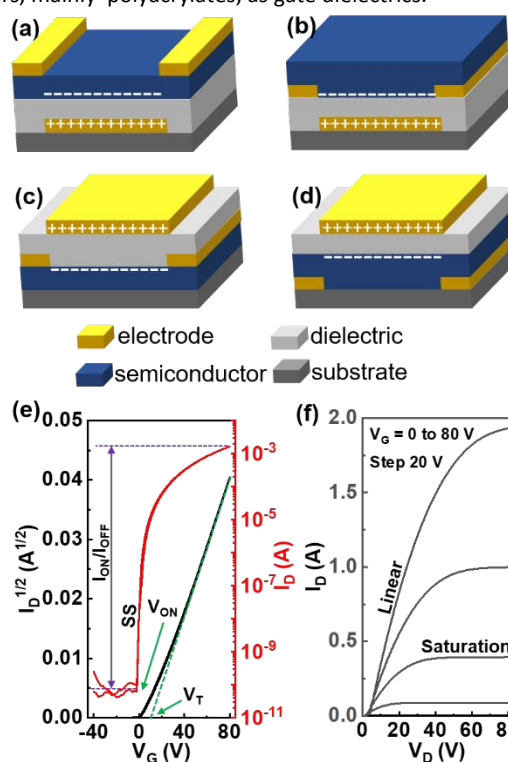


Figure 3. Thin-film transistor architectures operating with a n-type (positive charges) semiconductor: (a) bottom gate top contact (BGTC), (b) bottom gate bottom contact (BGBC), (c) top gate top contact (TGTC) and (d) top gate bottom contact (TGBC). Note, the illustration is based on n-type TFTs, where the accumulated electron carrier channel by a positive gate bias is presented. (e) Transfer and (f) output plots of an n-type (solution processed IGZO) TFT with indicated the linear and saturation regimes and how other relevant TFT performance parameters are measured.

The characteristic that best defines a TFT is the possibility to modulate the conductivity (or electrical current) of the channel between the source and drain electrodes by using two independent electric fields (or biases), one provided by applying a bias between the source and drain electrodes (V_D) and the second via the source and gate electrodes (V_G). Thus, assuming a given V_D , a positive/negative V_G will induce negative/positive charges at the insulator-semiconductor interface for n-type and p-type TFTs, respectively, and the number of the accumulated charges depends on both V_G and C_i of the gate insulator. Upon increasing both V_G and V_D , the current measured between the source and drain contacts (I_D) will increase following two different regimes which depends on the relative strength of V_D vs. V_G . Thus, in the linear regime, when $V_D \ll (V_G - V_T)$, I_D is given by eq. (7), while in the saturation regime, when $V_D > (V_G - V_T)$, it is given by eq. (8),

$$I_D = \mu C_i \frac{W}{L} \left[(V_G - V_T) V_D - \frac{V_D^2}{2} \right], \text{ when } V_D \ll (V_G - V_T) \quad (7)$$

$$I_D = \mu C_i \frac{W}{2L} (V_G - V_T)^2, \text{ when } V_D > (V_G - V_T) \quad (8)$$

where μ is the field-effect mobility, V_T is the threshold voltage, and W and L are channel width and length, respectively. The μ is one of the most important figures-of-merits of TFTs, while others are V_T , turn-on voltage (V_{ON}), I_{ON}/I_{OFF} ratio, and subthreshold swing (SS). These parameters can be extracted from the output (I_D - V_D) and transfer (I_D - V_G) plots (Figure 3e and f, respectively) and additional details of TFT operation and parameter extraction models can be found in previous reviews.^{44, 61}

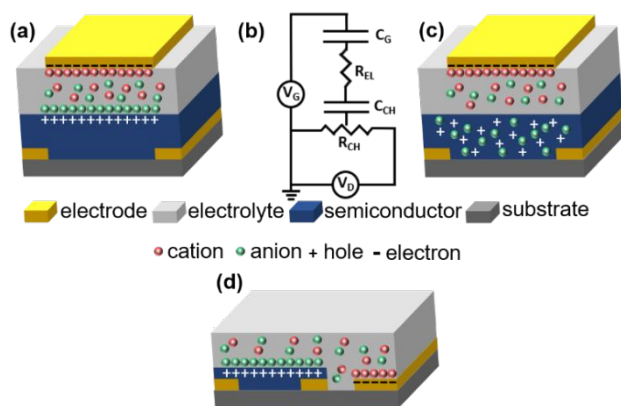


Figure 4. (a) Typical p-type EDLT structure with top-gate bottom contact geometry with a semiconductor that is impermeable to ions of the electrolyte. (b) A simplified equivalent circuit of an EGT. (c) Illustration of a p-type ECT structure with the distribution of cations and anions highlighted. (d) Illustration of a p-type EDLT with a side-gate structure.

When using an electrolyte as the gate dielectric in EGTs, the device architecture could be similar to those reported above for a TFT but since most studies employed liquid or gel electrolytes, bottom-contact geometries with a top-gate electrode are far more common. Typical semiconductors utilized in TFTs have also been adopted in EGTs, including undoped silicon,⁶² oxides,^{34, 63, 64} organics,^{49, 65, 66} and two-dimensional metal chalcogenides,^{27, 67} while source/drain electrodes are typically Au, carbon paste and

conducting polymers. Regarding the gate electrode, common metal electrodes have been used but non-polarizable and electrochemically active electrodes, such as Ag/AgCl and a PEDOT:PSS electrode, have been more commonly explored in recent years.^{62, 68}

There are two basic operation mechanisms for EGTs. In the case where the semiconductor layer is impermeable to the ions of the electrolyte and does not undergo an electrochemical reaction (Figure 4a), the application of a V_G leads to migration and accumulation of ions at the gate/electrolyte and the semiconductor/electrolyte interfaces. The ions at these interfaces screen the charges in the gate electrode and cause accumulation of carriers in the semiconductor channel. The result is that EDLs are formed at each interface. Double layer charging in these devices is similar to that of a field-effect in TFTs. Thus, EGTs with impermeable semiconductors or with electrolyte incapable to penetrate in to the semiconductor are typically called electric double layer transistors (EDLTs) and we will use this terminology in this review.³³

Figure 4b reports the simplified equivalent circuit model of an EGT showing that the total capacitance of the gate/electrolyte/semiconductor stack is the result of two C_{EDL} s in series (similar to that in Figure 2b), where C_G and C_{CH} are the C_{EDL} s at the gate side and semiconductor side, respectively, R_{EL} is the electrolyte resistance, and R_{CH} is the channel resistance that is modulated by C_{CH} . Upon the application of a V_G , the fraction of the V_G that drops across the channel is controlled by the nature and geometry of the gate electrode. For efficient gating, C_G must be more than ten times larger than C_{CH} , otherwise a large fraction of the applied V_G will drop at the gate/electrolyte interface. For conventional gate electrode based on metals, the common way to increase the capacitance is to enlarge the area of gate electrode, however such large gates can be technically difficult to implement for some applications; consequently, using a thick PEDOT:PSS electrode or a nonpolarizable electrode, such as Ag/AgCl, as the gate can help achieve a large C_G . In this case, the voltage drop at the gate/electrolyte interface is negligible, and effective gating is achieved.^{32, 57, 69-71}

To evaluate the performance of an EDLT, eqs. (7) and (8) are also applicable for the calculation of μ . However, since these equations depend on C_i and since the electrolyte dielectric capacitance is strongly frequency dependent due to relatively long τ , accurate extraction of μ in an EDLT can be challenging. A common way to minimize the calculated mobility error is to correlate the frequency of the V_G sweeping to the capacitance-frequency (C-F) characteristics of the electrolyte dielectric so that a more accurate capacitance can be used for the calculation of μ .³⁴ Thus, the transconductance (g_m) is a more commonly reported parameter for EGTs, and is defined by eq. 9:

$$g_m = \Delta I_D / \Delta V_G \quad (9)$$

which directly reflects the current sensitivity of the EGT to gate

Review

voltage variations, and circuits with EGTs have higher g_m would typically show superior amplification capability.

EGTs with ion permeable and redox-active semiconductors are called electrochemical transistors (ECTs). In the case of ECTs, electrolyte ions penetrate into the semiconductor under the application of a V_G , thereby changing the doping state of the semiconductor and hence its conductivity (Figure 4c). The capacitor formed here is not based on an EDL at the semiconductor/electrolyte interface but a volumetric capacitor (same as Figure 2e, with C^* typically larger than 10 F/cm^3).³² Note that not all semiconductors can function properly in the electrochemical regime since only those capable of redox processes/bulk ion uptake from the electrolyte within the electrochemical potential window of the electrolyte exhibit electronic conductance upon gating. Nowadays, the most adopted ECT semiconductors are organic polymers,^{69, 72, 73} and some electrochemically active oxides.^{22, 74} Typically, to evaluate whether an EGT is functioning as an EDLT or an ECT, impedance and/or cyclic voltammetry measurements are carried out.⁷⁵

Since during ECT operation ions from the electrolyte enter the channel layer and change the bulk electronic conductivity of the semiconductor, a more accurate qualification of ECT performance is typically by normalizing g_m based on the channel geometry:^{76, 77}

$$g_{m,norm} = \frac{L}{Wd_s} g_m \quad (10)$$

where d_s is the semiconductor film thickness. However, it is also found that $g_{m,norm}$ still depends on V_G (in saturation) according to eq. (11),⁴⁷

$$g_{m,norm} = \mu C^* (V_G - V_T) \quad (11)$$

Consequently, μC^* is also widely regarded as a major figure-of-merit in OEECTs.⁷⁸ In recent years, ECTs have been extensively investigated due to their outstanding g_m values and excellent compatibility to biological systems.^{29-32, 79}

Since ECTs and EDLTs function on different working principles, they possess different advantages. Due to high capacitance related to bulk electrochemical doping, high g_m and the high current densities that can be achieved in ECTs, they are ideal for small signal amplification in biosensors and electrochromic elements where large currents are needed. Conversely EDLTs typically exhibit a faster switching speed and smaller I-V hysteresis compared to ECTs, thus they are more suitable for integration in logic circuits where greater frequencies are required. Moreover, since the formation of the EDL and the volumetric capacitor are not limited by the geometry of the device/electrolyte, and considering that most of the electrolytes show excellent mechanical deformation, the structure of EGTs and the location of gate is not as restricted as in TFTs. Note, while in a conventional TFTs the gate is either on top or at the bottom of the semiconducting layer (Figure 3), EGT architectures can be side-gated (Figure 4d), making them ideal for various unconventional applications, including logic assembling with micro fluid channels/chambers,⁸⁰ logic circuits,⁸¹ interfacing on live tissues,⁸² and integration with textiles.⁸³

3. Electrolyte gate dielectric materials

Electrolyte materials with different chemical structure and physical state enable diverse EGT functionalities and are differently suitable for applications. Liquid-based electrolytes are mostly utilized in sensors, including biosensors and chemical sensors. Polymer-based electrolytes are most broadly used in EGTs, due to the tunable viscosity characteristics and processing temperatures enabling film processing with various fabrication coating and printing techniques. Furthermore, since polymer-based electrolytes are mostly in the solid-state, they enable efficient EGT circuit integration.⁸⁴ Inorganic electrolytes provide additional opportunities for EGTs thanks to their enhanced stability at high temperatures. In this section, we report the structure of several electrolyte material families, current development status, major properties, and potential applications.

3.1. Liquid electrolytes

Liquid electrolytes used in EGTs can be mainly divided into aqueous salt electrolytes (Type I) and ILs (Type II). Figure 5 reports the major salts used in aqueous electrolytes along with the chemical structure of common ILs used in EGTs. Note, water is by far the most utilized solvent in salt electrolyte, however, other solvents such as formamide, ethanol, and propylene carbonate have been investigated.^{85, 86}

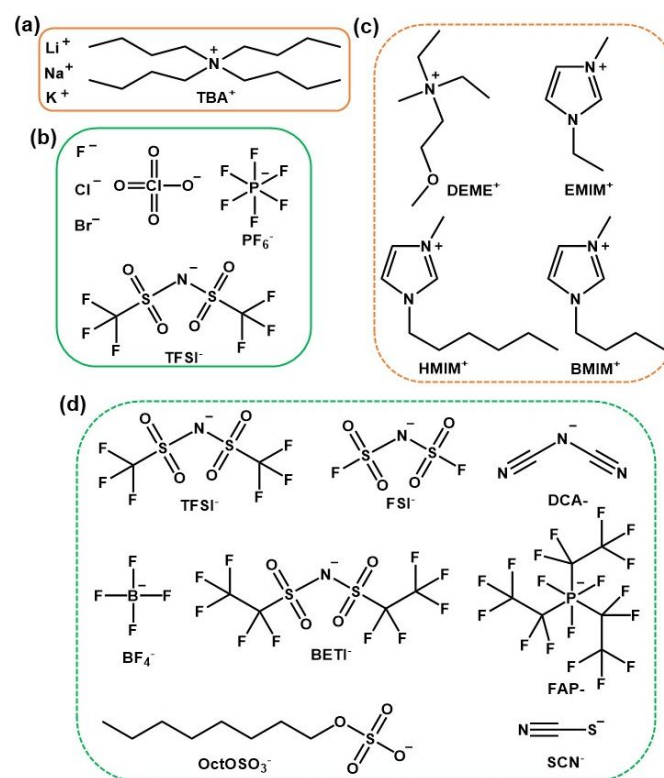


Figure 5. Representative liquid electrolyte chemical structures. (a) Cations and (b) anions of salts typically used in salt electrolytes. (c) Cations and (d) anions typically used of IL electrolytes.

3.1.1. Type I, aqueous salt electrolytes

The first demonstration of electrolyte gating was reported in 1955 using germanium as the semiconductor and 0.1 M KOH, KCl, or

HCl aqueous solutions,¹⁵ however, it was not until 1970 that the first functional transistor using an electrolyte (0.002 ~ 1 M NaCl aqueous solution) as gate dielectric was constructed. It consisted of an aqueous electrolyte with a SiO₂ layer acting as a series dielectric capacitor of a Si MOSFET.⁸⁷ This pioneer work is regarded as the first ion sensitive field-effect transistor (ISFET) and stimulated the development of EGTs.^{88,89,90}

After decades of development, the most common salts used in aqueous electrolytes include lithium bis(trifluoro-methanesulfonyl)imide (LiTFSI), sodium chloride (NaCl), potassium perchlorate (KClO₄), potassium hexafluorophosphate (KPF₆), and potassium chloride (KCl) (Figures 5a,b). Among them, bio-compatible electrolytes such as NaCl, KCl, and phosphate-buffered saline (PBS) solutions have been mostly adopted in EGTs for chemical/electrical physiological signal detection, bio-interfacing, and health monitoring.^{73, 91} Importantly, since OECTs are the devices mostly utilizing aqueous salt electrolytes, mechanistic studies addressing the influence of different salts on the electrochemical process largely promoted the development of high performance OECTs.

As OECT research progressed, several new polymer semiconductors were synthesized/utilized to facilitate ion diffusion in the organic active layer.⁹²⁻⁹⁴ Both high performance p- and n-type semiconducting polymers with stable electrochemical behaviour in aqueous electrolyte were reported by incorporating hydrophilic functional groups (e.g., ethylene glycol chains) on known semiconducting polymer backbones. However, the chemical structure of the salt used in the aqueous solution greatly affect the OECT performance in both traditional hydrophobic and newly developed hydrophilic polymers used as the semiconductor.

Ginger et al. first studied how the anion of different potassium electrolytes affects mixed ionic/electronic transport properties of poly(3-hexylthiophene-2,5-diyl) (P3HT) based OECTs.⁹⁵ The authors investigated 20 mM solutions of K⁺ salts including F⁻, Cl⁻, Br⁻, ClO₄⁻, PF₆⁻, or TFSI⁻. It was found that both I_D and V_T of P3HT based OECTs strongly depended on the anion type of the electrolyte, with the maximum I_D increasing and V_T decreasing in the following anion order: F⁻ → Cl⁻ → Br⁻ → ClO₄⁻ → PF₆⁻ → TFSI⁻ (Figure 6a). Surprisingly, it appeared that ion diffusion into, and doping ability of, P3HT for OECTs using electrolytes with bulkier anions, like PF₆⁻ and TFSI⁻, were more efficient than those based on smaller Cl⁻ and ClO₄⁻ (Figure 6b). These results were rationalized considering the negligible number of water molecules coordinating the large anions, which effectively reduced their ionic radii in solution. The same group carried out a similar study but using a more hydrophilic polymeric semiconductor, poly(3-[[2-(2-methoxyethoxy)ethoxy]methyl]thiophene-2,5-diyl) (P3MEEMT).⁹⁶ Since the ethylene glycol side chains facilitate the diffusion of anions, it was found that P3MEEMT based OECTs exhibited faster anion injection rates compared with those based on P3HT. Figure 6c reports the absorption spectra versus time of P3HT and P3MEEMT films upon electrochemical doping using either 0.1 M KCl and 0.1 M KPF₆ electrolyte solutions (V_G = 0.7 V and 0.5 s between spectra). For both polymers the neutral absorption peak decreases

with longer V_G bias time, along with an enhanced red-shifted polaron peak. When using PF₆⁻ as the anion, the neutral and polaron peaks decrease and increase more rapidly, respectively, for both P3MEEMT and P3HT, indicating a higher degree of doping rate compared to that measured using a Cl⁻ based solution. Representative transfer curves for OECTs with a P3MEEMT active layer with both electrolytes (Figure 6d) indicated that 5x higher drain current and transconductance were achieved with KPF₆ than with KCl. This difference originated from a ~126 mV decreased threshold voltage for KPF₆ compared to KCl. The resulting μC* of 96.7 ± 10.2 F cm⁻¹V⁻¹s⁻¹ for KPF₆ is ~ 2x higher than that (49.1 ± 5.0 F cm⁻¹V⁻¹s⁻¹) measured for KCl.

These studies demonstrated that regardless of the hydrophobicity of polymer the performance, and especially V_T, of p-type OECTs depend on the anion type of the aqueous electrolyte. In general, a smaller driving force for ion penetration into the semiconducting polymer is required for larger, less polarizable, anions with a lower surface charge density. This phenomenon could arise from a competition between ion hydration number and semiconductor polymer doping kinetic, where more chaotropic ions tend to dope the polymer more easily than more kosmotropic ions.

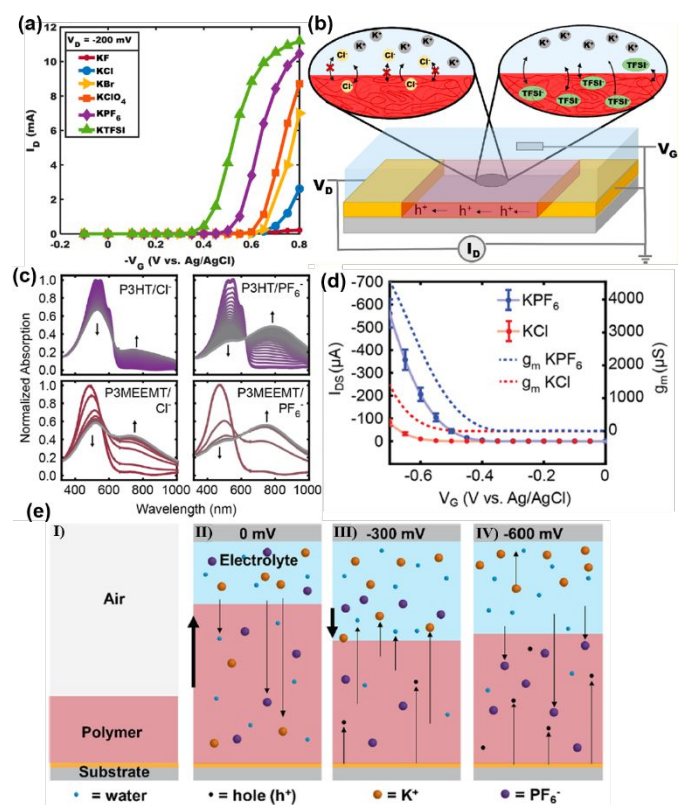


Figure 6. (a) Representative transfer curves of P3HT OECTs with six different aqueous electrolytes. (b) Schematic illustration showing that Cl⁻ is less intercalating than TFSI⁻. Reprinted with permission.⁹⁵ Copyright 2018, American Chemical Society. (c) UV-vis spectra of P3HT and P3MEEMT films upon electrochemical doping at 0.7 V in aqueous solutions of KCl and KPF₆ (0.5 s between spectra). (d) Transfer and transconductance curves of P3MEEMT OECTs in aqueous KCl and KPF₆ solutions. Reprinted with permission.⁹⁶ Copyright 2019, American Chemical Society. (e) Scheme illustrating the mechanism of electrochemical oxidation with KPF₆ under different voltage biases. Reprinted with permission.⁹⁷ Copyright 2020, American Chemical Society.

Review

Recently, Ginger et al. further investigated the mechanism of ion-dependent electrochemical oxidation (doping) of p-type OECTs on cations.⁹⁷ By adopting a combination of electrochemical quartz microbalance gravimetry and glow discharge optical emission spectroscopy, it was shown that charge compensation during polymer redox processes is also cation dependent. As shown in Figure 6e, after a P3MEEMT film is immersed into the KPF₆ electrolyte solution, swelling occurs even without applying any bias voltage. The authors pointed that water, K⁺, and PF₆⁻ diffused into the bulk of the polymer film (Panel II) at 0 mV bias; when a relatively low negative bias (-300 mV) was applied, part of the water and most of the K⁺ were expelled from the film (Panel III); using a higher bias (-600 mV) would then further lead to more anion penetration and higher oxidation/doping levels (Panel IV). Note, using the bulkier tetrabutylammonium hexafluorophosphate (TBAPF₆, see Figure 5a for the molecular structure), negligible/little cation transport into the film is observed. More interestingly, when using KCl and tetrabutylammonium chloride (TBACl) as electrolytes, no obvious cation injection before or during the bias scan is observed, indicating both anion and cation determine the swelling process of the polymer. It was suggested that this was due to the large solvation shell of Cl⁻, which inhibited the injection of both ions.

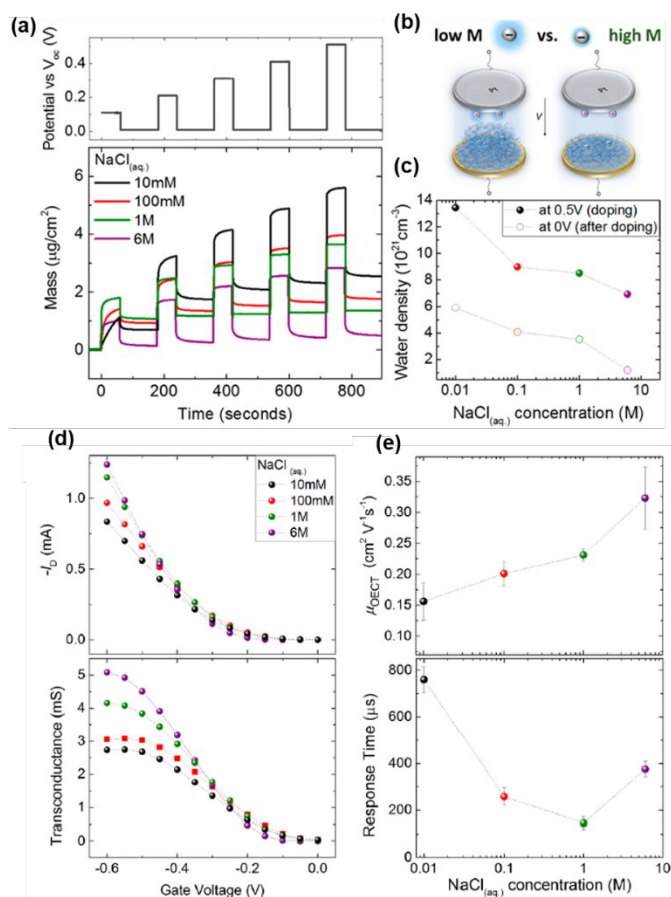


Figure 7. (a) Applied potential waveform as a function of time, and changes in the mass of the films when doped with four electrolytes of varying ion concentrations. (b) Schematic representation of p(g2T-TT)-NaCl(aq) system in the EQCM-D chamber during doping at low and high electrolyte concentrations. (c) The number of water molecules injected into the films at the end of the doping pulse at 0.5 V

and remaining in the film upon the subsequent dedoping pulse applied at 0 V as a function of NaCl concentration. (d) Transfer and transconductance plots of p(g2T-TT) OECTs with different NaCl concentrations. (e) Hole mobility of p(g2T-TT) film as a function of the NaCl(aq) concentration, and response time of the OECTs as a function of the NaCl concentration measured at $V_G = V_D = -0.5$ V. Reprinted with permission.⁹⁸ Copyright 2019, American Chemical Society.

Another important factor that can impact the property of an aqueous electrolyte for OECTs is the salt concentration since it influences solvation shell properties and electrochemical behaviour of the electrolyte.⁵¹ By using different NaCl concentrations in water (10 mM ~ 6 M) as electrolytes, Inal et al. quantified the amount of water and dopant anion that incorporated into an hydrophilic p-type semiconductor film [p(g2T-TT)] as well as investigated structural and morphological changes during the electrochemical doping process.⁹⁸ The oscillation frequency and dissipation of energy overtone from Electrochemical Quartz Crystal Microbalance with Dissipation Monitoring (EQCM-D) were carefully monitored when the potential pulse on p(g2T-TT) films was applied with the electrolyte having different NaCl concentrations and transformed into mass changes (Figure 7a). When the polymer is doped in the presence of the more diluted NaCl(aq), the semiconductor film gained more mass when applying the same potential (Figure 7b). For instance, the p(g2T-TT) film mass increased by 86% and 42% at 0.5 V (voltage bias the p(g2T-TT) film side), when using 10 mM and 6 M NaCl(aq) electrolytes, respectively. In addition, when the potential was reverted to 0 V, a fraction of the incorporated mass remained in the film, which was higher for the film in contact with the electrolyte with a lower NaCl concentrations (Figure 7c). Since the charge density directly corresponds to the number (mass) of doping anions in the film while the mass calculated from the injected anions is smaller than the measured mass, this discrepancy corresponds to the mass of water being incorporated into the polymer film. Interestingly water uptakes increased with decreasing the electrolyte concentration, which was rationalized by the larger degree of anion hydration. Moreover, a fraction of water remained in the film even after the dedoping pulse (bias = 0 V), and this was most pronounced when using more diluted NaCl solutions. The authors pointed that in the solution osmosis also plays an important role in determining water drift since it is the greatest when using NaCl(aq) 10 mM due to the maximized difference in solute concentration between the electrolyte and the film. These results evidenced two important phenomena regarding the doping process in a p-type organic semiconductor using aqueous electrolytes: (1) The anions that enter the semiconductor film are hydrated; (2) The semiconductor film swells more upon uptake of anions from a low concentration electrolyte solution, thus retaining water more efficiently in these conditions. The authors also investigated the corresponding p(g2T-TT) OECTs with different NaCl concentrations (Figure 7d). Both I_0 and g_m were always greater at higher NaCl concentrations. Moreover, the hole mobility was found to scale with the NaCl concentration as: $\mu = 0.15, 0.20, 0.22,$ and 0.33 cm²/Vs when NaCl(aq) = 10 mM, 100 mM, 1 M, and 6 M, respectively (Figure 7e). The extent of semiconductor swelling also influenced the OECT transient characteristics, with the OECTs gated in NaCl(aq) 1 M switching ON more efficiently, while the

slowest response was predominantly measured in NaCl(aq) 10 mM. At the highest NaCl(aq) concentration (6 M), the low ion hydration led to greater ion pairing forces which opposed injection of Cl^- ions into the film to compensate for polarons. Therefore, the OECTs gated with NaCl(aq) 6 M switch ON slower compared with 1 M. The authors also showed that infiltration of the hydrated ions into the film irreversibly changes the polymer structure and negatively impacts the efficiency, reversibility, and speed of charge generation. When less water was incorporated into the device channel the OECTs exhibited higher transconductance and faster switching speeds.⁹⁹ Although semiconductor swelling is thought to be a necessity for efficient ion to electron transduction, these studies uncovered the negative impact of a swollen semiconductor on the performance of accumulation mode OECTs and laid the foundation for future materials design/screening not only for semiconductors but also electrolytes.^{97, 100, 101}

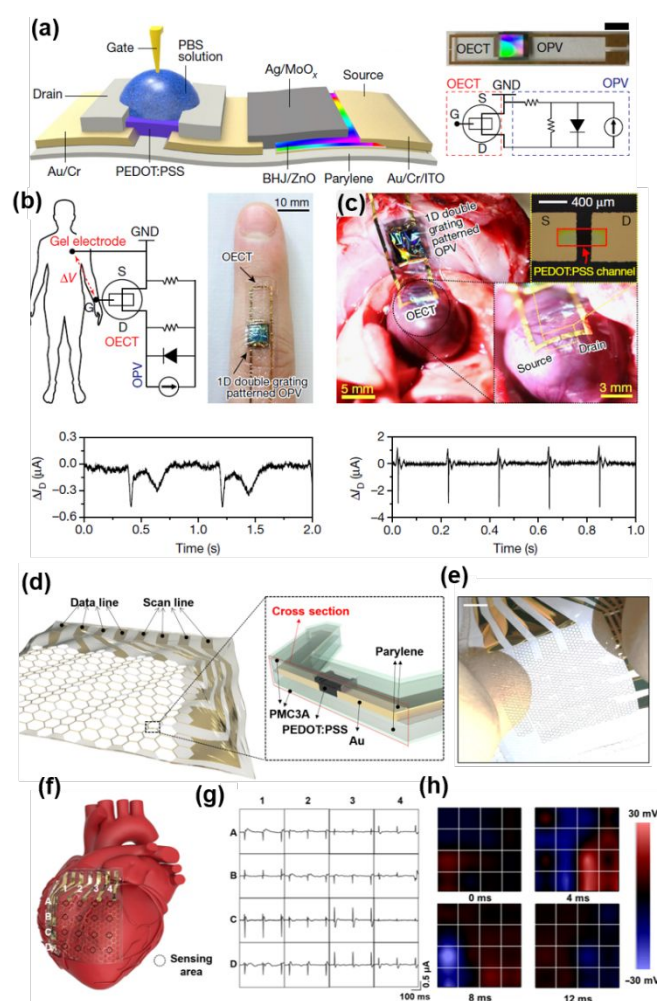


Figure 8. (a) Schematic of an OPV integrated with an OECT, along with a photograph of the integrated device (Scale bar, 5 mm) and the corresponding circuit diagram. (b) Wiring diagram for cardiac signal recording and a photograph of the self-powered integrated electronic device attached to a finger. The lower panel shows the measured output current from the recorded cardiac signal trace under light illumination. (c) Photograph of the self-powered integrated electronic device attached to the heart of a rat (left), and enlarged images of the channel area (right, top) and of the source–drain electrode (right, bottom), along with the

measured output current from the ECG trace, under light illumination. Reprinted with permission.¹⁰² Copyright 2018, Springer Nature. (d) Stretchable OECT array on honeycomb grid substrate, and cross section of the stretchable OECT array. (e) A 4×4 stretchable OECT array when intrinsically stretched (Scale bar, 3 mm). (f) Image of the positioning of and (g) ECG signals from the 4×4 OECT array on the heart of a rat, along with (h) Time delay of ECG signals. Reprinted with permission.¹⁰³ Copyright 2018, The American Association for the Advancement of Science.

Due to the liquid nature and excellent bio-compatibility of most aqueous salts, EGTs based on these electrolytes have been investigated for physiological sensing and health monitoring.^{104–106} Furthermore, due to the ultra-high transconductance, low driving voltage and low power for operation, considerable efforts has been made in using OECTs in the area of self-powered electronics.^{102, 107} For instance, Someya et al. combined flexible organic photovoltaic cells (OPVs) with OECTs and realized self-powered ultra-flexible electronic devices that can adhere to moveable and complex three-dimensional biological tissues to measure biometric signals with very high signal to-noise ratios (Figure 8a).¹⁰² In this study, a physiological PBS solution was first used as the aqueous electrolyte for OECTs demonstrating a conformal self-powered cardiac sensor using OECTs as the sensing elements. The device was mounted on a human fingertip and consisted of gold contacts, a PBS electrolyte and PEDOT:PSS as channel material and it had the OECT source electrode grounded with a gel-electrode attached to the human chest (Figure 8b). The potential difference between the gel electrode on the chest and the OECT channel on the fingertip acts as the gate bias, affecting the PEDOT:PSS channel conductance. Consequently, clear biological signal curves were detected with the OPV under LED light illumination providing electrical power to drive the OECT. The peak intensity and standard deviation of the recorded OECT I_D , which is induced by the cardiac signal, were $0.47 \mu\text{A}$ and 23.5 nA , respectively, resulting in a calculated signal-to-noise ratio of 25.9 dB. Taking advantage of the mechanical flexibility and bio-compatibility of this OECT, the fabricated device was further attached to the exposed surface of a rat heart, where the body fluid on the heart surface acted as the electrolyte (Figure 8c). The electrocardiographic (ECG) signals of the rat heart, due to the heart-action-evoked potential, were measured under the LED illumination and exhibited strong ECG signals with an amplitude of $2.96 \mu\text{A}$ and a standard deviation of 25.2 nA , resulting in a signal-to-noise ratio of 40.02 dB.

The liquid state of aqueous electrolytes can simplify EGT integration in sensing arrays.¹⁰⁸ For instance, a stretchable multielectrode array consisting of (4×4) OECTs, which is similar to that of an active matrix structure in flat panel display (including a data line and scan line), was fabricated on a $1.2\text{-}\mu\text{m}$ -thick parylene substrate (Figure 8d).¹⁰³ The total thickness was as thin as $2.6 \mu\text{m}$, including the top encapsulation of a $1.2\text{-}\mu\text{m}$ -thick parylene layer, resulting in highly flexible and stretchable structure. Cross section of the stretchable device (Figure 8d) evidences layers of PEDOT:PSS and source/drain gold electrodes deposited on a honeycomb grid substrate. The honeycomb grid substrate was chosen due to its mechanical stability and structural stretchability (Figure 8e). Note, the outermost layers are made of poly(3-methoxypropyl acrylate) (PMC3A), which provide high blood compatibility. The 4×4 array was

attached to the exposed surface of the heart of rats to measure physiological signals (Figure 8f). The conformal contact between the device film and the surface of the heart was possible by the use of honeycomb holes on the ultrathin substrate. The result of the spatial distribution of the recorded ECG outputs are shown in Figure 8g. Spatial voltage maps of all nodes at four sequential time points are

reported in Figure 8h. The anatomical signals show different shapes based on the location of the sensors. The OECT array successfully recorded spatial-temporal distribution of ECGs on the heart surface with multiplexing. Consequently, high-precision monitoring of electrophysiological signals with high spatial and temporal resolutions was realized with the stretchable OECT array.

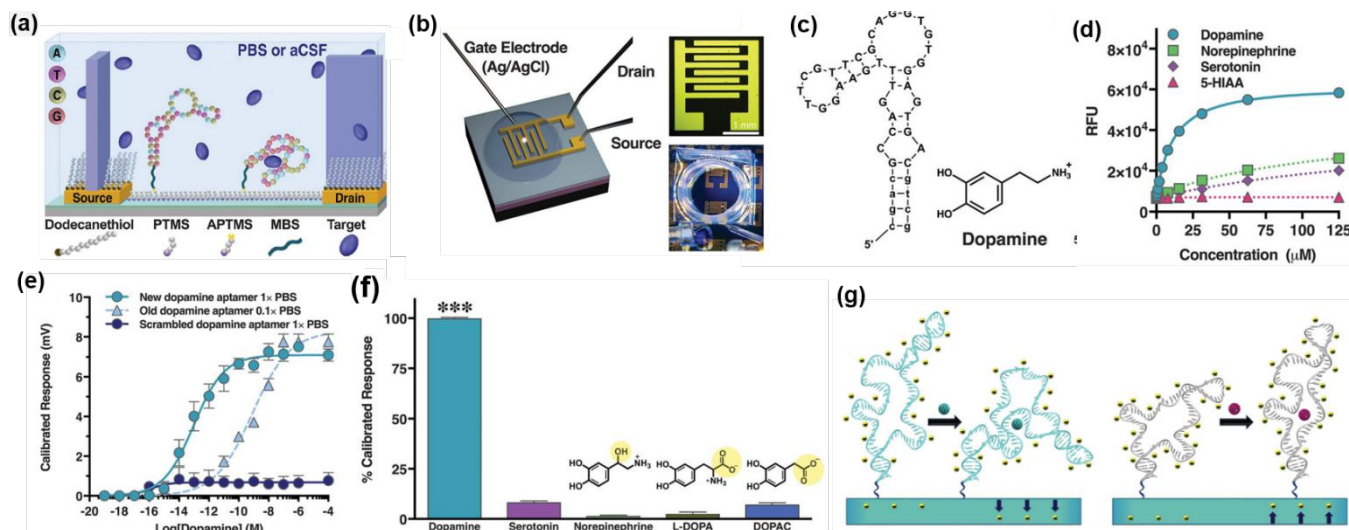


Figure 9. (a) Schematic of EDLT surface chemistry, where PTMS is trimethoxy(propyl)silane; APTMS is (3-aminopropyl)trimethoxysilane; MBS is 3-maleimidobenzoic acid *N*-hydroxysuccinimide ester, along with (b) EDLT microscope image, and photograph of experimental setup. (c) Aptamers for dopamine, and (d) fluorescence-concentration curves (RFU, relative fluorescence units) indicate selectivity of dopamine aptamers versus nonspecific targets. (e) Responses of EDLT sensors functionalized with the dopamine aptamer or its scrambled sequence, compared to EDLT responses with a previously reported dopamine aptamer, along with (f) the selectivity of the EDLT. (g) Hypothesized mechanism of stem-loop aptamer target-induced reorientations in close proximity to semiconductor channels and within or near the Debye length: (Left) Aptamers reorient closer to EDLTs to deplete channels electrostatically; (Right) aptamer stem-loops reorient away from the semiconductor channel, thereby increasing transconductance. Reprinted with permission.¹⁰⁹ Copyright 2018, The American Association for the Advancement of Science.

The above studies demonstrated the advantages of adopting OECTs as sensing elements for electrophysiology. Chemical physiological signals can also be detected by proper design of EGTs with functional electrolytes and/or interface engineering.¹¹⁰⁻¹¹³ For instance, by introducing different aptamers on a solution processed nanometer-thin In_2O_3 film (Figure 9a), Andrews et al. developed EDLTs that bypassed the EDL shielding effect and realized devices that are extremely sensitive to several important analytes in PBS (Figure 9b), including dopamine, serotonin, glucose, and sphingosine-1-phosphate (S1P).¹⁰⁹ Note, EDL shielding effect means that in ionic solutions the EDL shields the semiconductor charge carriers to limit gating in response to recognition events, and the extent of shielding (i.e., the effective sensing distance) is characterized by the Debye length, which in physiological fluids is <1 nm. An example of an aptamer for dopamine is shown in Figure 9c. This molecule exhibits high sensitivity and selectivity to dopamine based on fluorescence responses (Figure 9d). With such aptamer, the device was responsive to a wide range of dopamine concentrations (10^{-14} to 10^{-9} M) in physiological PBS (Figure 9e). Importantly, dopamine aptamer-EDLTs were selective to dopamine versus serotonin, norepinephrine, and tyramine as well as dopamine metabolites (Figure 9f). Note, a specific aptamer for each analyte was adopted to yield high sensitivity and selectivity. The hypothesized mechanism involves analyte-induced reorientation of the aptamer in

close proximity to the semiconductor channel and within, or very near to, the Debye length. As shown in Figure 9g (left), for dopamine and glucose, the transfer curves are consistent with aptamer reorientations occurring such that a substantial portion of the negatively charged backbone moves closer to the n-type semiconductor channel, thereby increasing the electrostatic repulsion of the charge carriers, and thus decreasing the transconductance. In contrast, it is hypothesized that serotonin and S1P aptamers move predominantly away from channel surfaces upon analyte capture, thereby increasing the transconductance (Figure 9g, right).

3.1.2. Type II, ionic liquid electrolytes

ILs are salts that are in the liquid phase at room temperature and have several advantages compared to aqueous salt electrolytes such as absence of a solvent, larger electrochemical window (~ 3 V), low melting point (typically < -20 °C) and high boiling point (typically > 400 °C). Consequently, IL electrolytes are typically preferred compared to aqueous electrolytes especially when bio-compatibility is not required. Representative IL structures used in EGTs are shown in Figure 5, where the most common cations include diethylmethyl(2-methoxyethyl)ammonium (DEME⁺), 1-ethyl-3-methylimidazolium (EMIM⁺), 1-butyl-3-methylimidazolium (BMIM⁺),

and 1-hexyl-3-methylimidazolium (HMIM⁺), while the anions are bis(trifluoromethylsulfonyl)imide (TFSI⁻), bis(fluorosulfonyl) imide (FSI⁻), dicyanamide (DCA⁻), tetrafluoroborate (BF₄⁻), bis(pentafluoroethylsulfonyl)imide (BETI⁻), tris(pentafluoroethyl)-trifluorophosphate (FAP⁻), n-octylsulfate (OctOSO₃⁻), thiocyanate (SCN⁻). Note, there are several other IL structures not list here and that can be found in specialized publications.^{39, 40}

capacitance differed by two orders of magnitude upon anion variation and ranging from as high as 170 μF/cm² for [EMIM][DCA] to as low as about 5 μF/cm² for [EMIM][FSI] at 0.1 Hz. The large capacitance difference was attributed to different molecular arrangements of the cations and the anions in the EDLs as well as to their slower dynamics such as collective polarization of the molecular clusters. Rubrene EDLTs with the ILs and OFETs with an air gap as gate dielectric demonstrated that the large IL capacitance led to much high carrier density in the channel when using [EMIM][DCA] (~5.3×10¹⁴/cm²), which was 50 times higher than that of typical SiO₂ based devices (Figure 10b). However, the devices based on the ILs with a higher capacitance (e.g., [EMIM][DCA]) showed a significantly lower hole mobility (0.01 cm²/Vs) than those with a lower capacitance (e.g., [EMIM][FSI], μ = 9.5 cm²/Vs). Similar trends where the mobility decreases with increasing the gate insulator dielectric constant were reported for OFETs based on conventional gate dielectrics.^{61, 119} This result was attributed to polaronic self-localization of the charge carriers (Fröhlich polarons) at the semiconductor/dielectric interface due to the interaction with the highly polarizable gate dielectric material. Similarly, high capacitance ILs could also introduce coupling of the carrier motion in the vicinity to the EDLs.

Fukui et al. recently investigated the detail of charge trapping mechanism in IL gated EDLT using [EMIM][TFSI] as the electrolyte and a single crystal rubrene as the semiconductor.¹¹⁵ The time course of the linear transfer curves of the EDLT are shown in Figure 10c. After 540 min of the initial carrier injection, the transfer curve shifted by -0.11 V but without variation of the slope of the linear region as well as the width of the subthreshold region. This result was similar to that of a bias stressed p-type OFET exhibiting a negative V_T shift, where carriers (holes) were trapped in the organic semiconductors.¹²⁰⁻¹²⁴ Figure 10d shows the time course of the normalized I_D [I_D(t)/I₀, I₀ = I_D(t = 0 s)] measured at V_G = -0.3 V. When a large OFF-state (V_G > V_{turn-on}) gate voltage (V_G = 1.5 V) was applied, the linear transfer curve shifted back to the initial position, signature of a carrier detrapping process. After detrapping, the linear transfer curve gradually shifted to the negative direction again on the same time scale as that before detrapping, indicating that this bias stress process was reversible. By using electrochemical frequency modulation, atomic force microscopy and molecular dynamic (MD) simulations, the authors suggested a gradual structuring of the first IL layer facing the carriers injected in the rubrene surface leading to ion reorientations and electrostatic stabilization by forming a patchwork structure (Figure 10e). In this stable configuration, negatively charged O and F atoms of the FSI⁻, pointing to the positively charged rubrene surface, come closer and lead to the gradual hole carrier trapping (Figure 10e). Moreover, when a large positive gate voltage was applied, such structured IL layer would be deformed and IL-induced bias stress recovered immediately by detrapping the hole carriers.

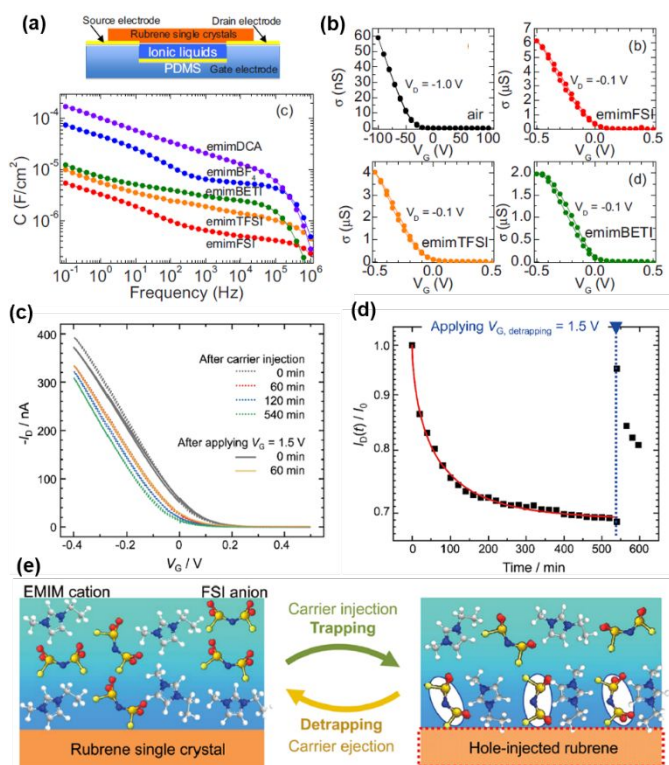


Figure 10. (a) Structure of an EDLT based on an organic single crystal semiconductor and an IL as gate dielectric (top) and capacitance of the indicated ILs as a function of frequency measured by impedance technique (bottom). (b) Transfer characteristics of EDLTs with an air-gap, [EMIM][FSI], [EMIM][TFSI], and [EMIM][BETI] as the gate dielectrics (V_D = -0.1 V). Reprinted with permission.¹¹⁴ Copyright 2009, AIP Publishing. (c) Time course of linear transfer curves of EDLT based on [EMIM][FSI] (V_D = -0.1 V and scan rate = 20 mV/s). (d) Time course of the normalized I_D measured at V_G = -0.3 V (black squares). The red solid line is the fitted data. The blue dotted line represents the time when the detrapping gate voltage (V_{G,detrapping} = 1.5 V) was applied. (e) Schematic of the carrier trapping and detrapping dynamics by FSI anions in the first IL layer. Reprinted with permission.¹¹⁵ Copyright 2020, American Chemical Society.

Even though ILs have been widely adopted in electrochemical mechanical actuators and electrochromic windows,¹¹⁶ the development of IL as gate dielectric of transistors only started in 2007, when Hebard et. al. used [EMIM][BETI] to gate indium oxide EDLTs.¹¹⁷ In 2008, Takeya et al. investigated rubrene single-crystal based EDLTs with various IL electrolytes such as [EMIM][TFSI], [EMIM][FSI], [EMIM][BF₄], and [EMIM][DCA] (Figure 10a).^{114, 118} The dielectric response of the ILs was measured in a Au/IL/Au capacitor structure in the frequency range from 0.1 Hz to 1 MHz. For all ILs the capacitance was found to increase when the frequency decreased particularly in the frequency range of 10 – 1 kHz because of the slow rotational rearrangement of the ionic molecules. Specifically, the

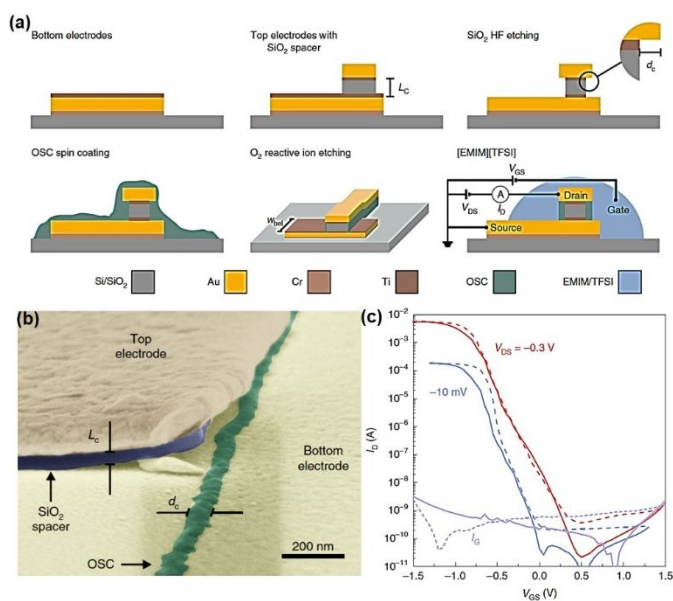


Figure 11. (a) Vertical EDLT fabrication process. (b) Colored cross-sectional SEM image near the edge of the vertical device. (c) Transfer characteristics of a PDPP based vertical EDLT measured in ambient atmosphere. The solid lines represent the trace and the dashed lines are re-trace. Reprinted with permission.¹²⁵ Copyright 2019, Springer Nature.

The liquid nature of ILs can also be used to gate unconventional device/channel architectures where solid dielectrics would be

difficult to conformally contact the semiconductor. Thus, Okaue et al fabricated vertical channel EDLTs with a channel length as short as 40 nm which can be easily accessible to the IL.¹²⁵ The device fabrication process and resulting structure is reported in Figure 11a and consisted of gold source and drain electrodes, patterned by electron beam lithography, and spaced by a sputtered SiO₂ layer, defining the device channel length ($L = \text{thickness of SiO}_2$). An under-etched space was realized with HF etching, and then was filled by the semiconductor (a diketopyrrolopyrrole-terthiophene donor-acceptor polymer, PDPP) which was deposited by spin-coating and patterned by O₂ reactive ion etching. Note, Cr and Ti were used for better adhesion between Au and SiO₂. A cross-sectional SEM image of the device cut through the transistor channel (before contacting the electrolyte-gate pair) is reported in Figure 11b, where a well-defined organic semiconducting polymer channel can be observed. The EDLT was then completed by using [EMIM][TFSI] as the dielectric. Typical transfer curves of this device are shown in Figure 11c, where a large $I_{\text{ON}}/I_{\text{OFF}}$ ratio of up to 10⁸ is observed, along with a large on-current of $\sim 10^{-3}$ A at extremely low V_D (-0.3 V) and V_G (< 1.5 V) biases. This performance corresponds to a high current density in the range of 10⁴ – 10⁷ A/cm² when only accounting the area of the semiconducting materials, a remarkable value for organic transistors.

3.2. Polymer-based electrolytes

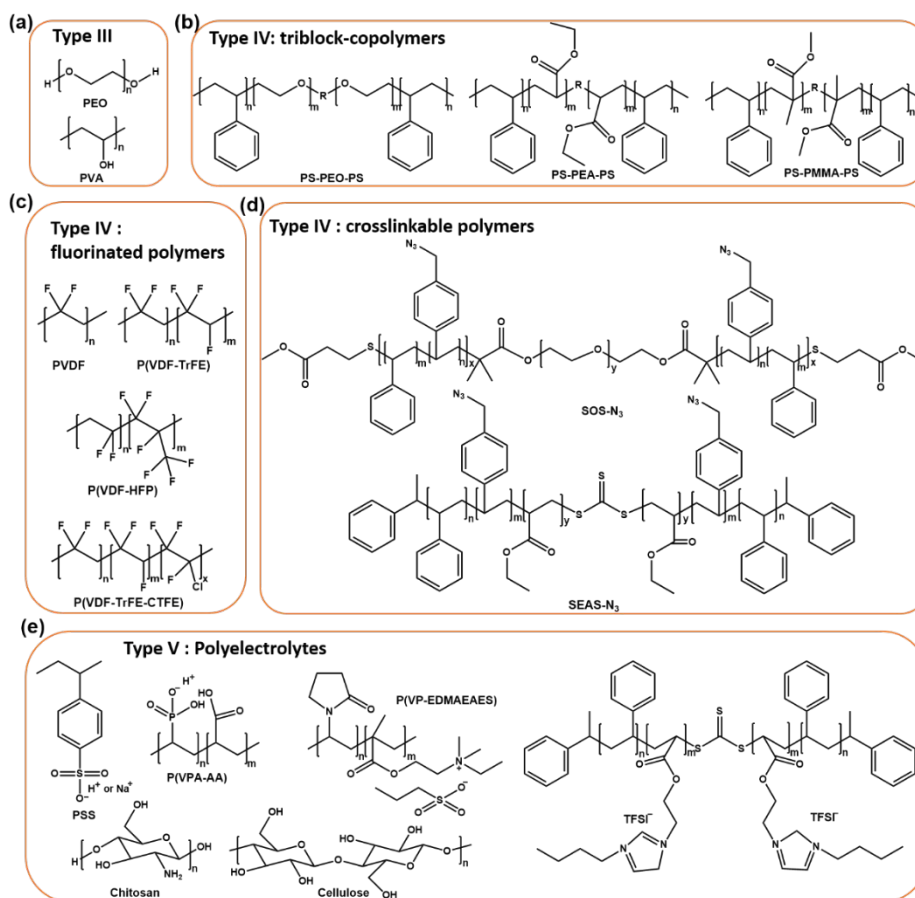


Figure 12. Representative chemical structures of polymers used in polymer-based electrolytes. (a) Polymers for polymer electrolytes; (b-d) polymers for ion gel, where (b) are triblock-copolymers, (c) are fluorinated polymers, and (d) are representative copolymers (SOS-N₃ and SEAS-N₃) with photo crosslinkable units; (e) Polyelectrolytes.

Typical insulating polymers do not transport electronic charge and, if pure, do not contain ions and will not form an EDL upon the application of a voltage bias. Thus, these materials are usually excellent gate dielectrics for transistors of different structures.¹²⁶⁻¹³⁰ To enable polymer based electrolytes, ions must be added to, or incorporated into, the polymer structure typically via three strategies, which result in the following classes of polymer based electrolytes: 1) Polymer electrolytes (Type III), obtained by mixing a salt with a polymer resulting in a solid solution; 2) Ion gel electrolytes (Type IV), obtained by mixing a salt, typically an IL, with a polymer resulting in a gel; and 3) Polyelectrolytes (Type V), which are polymers containing charged or ionizable groups. Representative polymers employed in the above-mentioned families are illustrated in Figure 12.

3.2.1 Type III, polymer electrolytes

Polymer electrolytes typically consist of a salt dissolved in an ion coordinating polymer (Figure 2c). The most studied coordinating polymer in this family is poly(ethylene oxide) (PEO), since the oxygen lone pairs on the PEO backbone efficiently coordinate positive ions, leading to a strongly coupled ionic motion and polymer backbone reorganization when an electric field is applied.¹³¹⁻¹³³ Other polymers, including poly(vinyl alcohol) (PVA)¹³⁴⁻¹³⁶ and polycarbonates (PCs),¹³⁷ have also been utilized (Figure 12a). Most of the salts used for aqueous electrolyte solutions can be used in polymer electrolytes (Figure 5), although the most frequently adopted one is LiClO_4 .^{132, 135, 138-140} Polymer electrolytes are prepared by dispensing a polymer + salt solution on the area of interest and drying it. It is worth noting that, since a polymer is used in these formulations, the rheological properties of the solution can be tuned, and controlled, to a great extent than those of aqueous and IL electrolytes (Types I and II) making them more suitable for several different processing techniques and, as different as, inkjet printing, spin-coating, and aerosol jet printing.

The first work reporting a polymer electrolyte as gate dielectric of a transistor was carried out in 1987 and was based on a side-gate transistor geometry using $\text{LiCF}_3\text{SO}_3 + \text{PEO}$ as the polymer electrolyte and P3HT as the semiconductor.^{141, 142} Compared to liquid electrolytes, the solid-state nature of polymer-based electrolytes enables efficient integration into circuits and enhanced stability while retaining a geometry suitable for EDL formation.¹⁴³⁻¹⁴⁶ Dasgupta et al. investigated high performance EDLTs based on a single-crystal ZnO nanowire semiconductor and an inkjet-printed polymer electrolyte dielectric consisting of PVA:propylene carbonate: $\text{LiClO}_4 = 20:63:7$ in mass, where the propylene carbonate acted as a plasticizer (Figure 13a).¹⁴⁷ These ZnO EDLTs operated at low voltages (≤ 2 V) and exhibited a high μ of $62 \text{ cm}^2/\text{Vs}$, $I_{\text{ON}}/I_{\text{OFF}}$ ratio of 10^7 , g_m of $155 \mu\text{S}/\mu\text{m}$, and a SS of $115 \text{ mV}/\text{dec}$. Moreover, as shown in Figure 13b, the EDLT transfer characteristics show minor variations (e.g. $\Delta V_T < 0.2 \text{ V}$) after storage in air for 20 days. The same group also utilized the same polymer electrolyte to fabricate all-printed IGZO EDLTs, and integrated them to demonstrate resistor (R-mode), enhancement type (E-mode), and depletion type (D-mode)

loaded inverters (Figure 13c).¹³⁸ Among all these devices, the E-mode based inverter showed the highest gain of about 3 for a low driving voltage of 0.5 V (Figure 13d). Note, even though the inverter performance based on all these modes were not ideal, it demonstrated the possibility of using polymer electrolyte as functional dielectrics in more complex circuits.

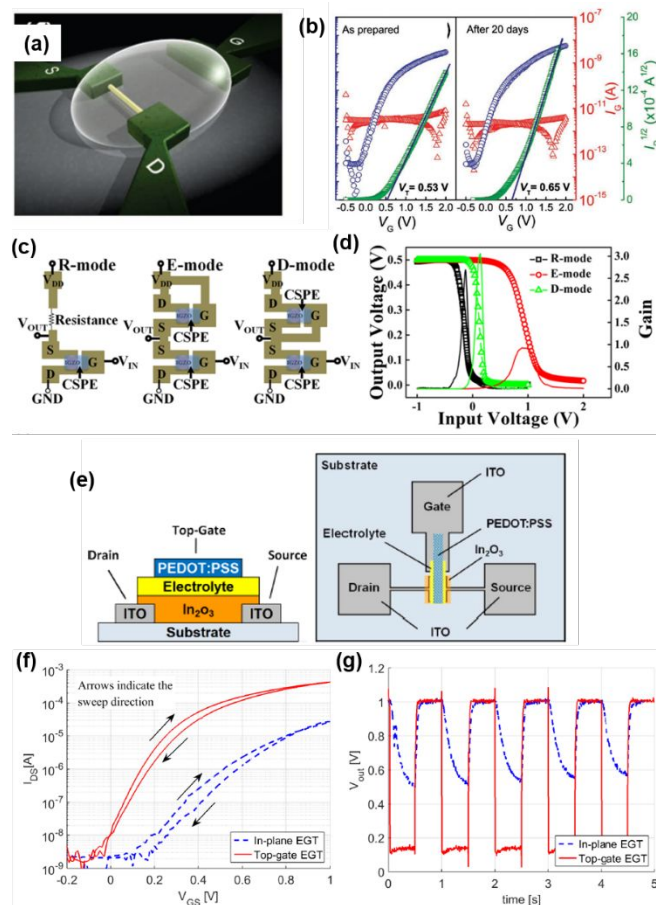


Figure 13. (a) Schematic representation of a ZnO nanowire EDLT using an inkjet-printed polymer electrolyte dielectric. (b) Representative transfer curves of ZnO nanowire EDLTs measured immediately after device fabrication and after 20 days stored in the air. Reprinted with permission.¹⁴⁷ Copyright 2013, John Wiley and Sons. (c) Schematic representations of IGZO-EDLT based logic inverter circuits using three different types of loads: a resistor (R-mode), an enhancement type (E-mode), and a depletion type (D-mode). (d) The corresponding voltage transfer and gain characteristics. Reprinted with permission.¹³⁸ Copyright 2018, American Chemical Society. (e) Cross-sectional and top views of a top-gate EDLT based on In_2O_3 . (f) Comparison of the transfer characteristics of an in-plane EDLT (sweep rate: $10 \text{ mV}/\text{s}$) with a top-gate EDLT (sweep rate: $2 \text{ mV}/\text{ms}$) at $V_{\text{DS}} = 1 \text{ V}$. (g) Comparison of the measured transient behavior of a resistor loaded inverter with an in-plane EDLT and a top-gate EDLT measured at $V_{\text{DD}} = 1 \text{ V}$. Reprinted with permission.¹⁴⁸ Copyright 2017, IEEE.

As mention in Section 2, electrolyte dielectrics enable the utilization of side-gate architectures (Figure 4d), which are much easier to fabricate compared to top gate structures (Figure 4a), and are widely adopted in EGT based sensors.¹⁴⁹ However, these devices suffer from slow switching, and thus low frequency of operation, since the gate-channel distance in these EGT architectures can be several μm s or more and thus, according to eq. (6), the polarization

time is large. In order to reduce the polarization time, the performance of a side-gate indium oxide (In_2O_3) EDLT was compared with that of a top-gate bottom-contact In_2O_3 EDLT with a printed PEDOT:PSS gate electrode and printed PVA/propylene carbonate/ LiClO_4 polymer electrolyte (Figure 13e).¹⁴⁸ Note, printing a gate on top of a liquid electrolyte is not conceivable but when using a solid polymer electrolyte is possible. As shown in Figure 13f, the transfer characteristics of the EDLT were measured with the side-gate (ITO gate electrode, which is in-plane with source and drain ITO electrodes) and remeasured after printing the PEDOT:PSS top-gate

(Figure 13e). Clearly, a considerably enhanced I_D along with a V_T of only ~ 0 V were obtained in this device configuration due to improved electrostatic coupling even when the sweeping speed of V_G for the top-gate EDLTs (2 V/s) is much greater compared to that (10 mV/s) of the side-gate devices. The voltage output curves were recorded in a resistor ($R = 19$ k Ω) loaded inverter. With a 1 Hz rectangular V_{IN} (0 and 1 V), the delay time decreases significantly from around 110 to 0.8 ms for the top-gate device, along with a much smaller voltage of the low level V_{OUT} (Figure 13g).

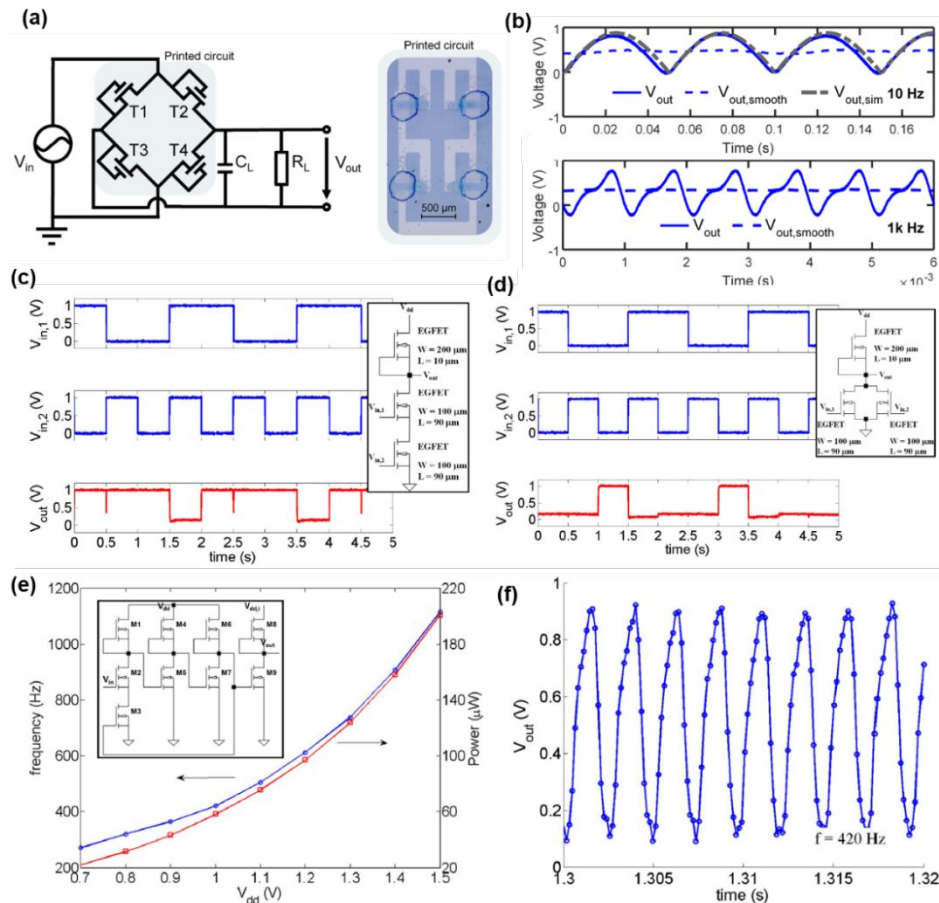


Figure 14. (a) Full-wave rectifier schematic, and a photograph of a diode-connected EDLT based full-wave rectifier. (b) Waveform of the measured V_{OUT} and smoothed output voltage ($V_{OUT,smooth}$) using a load capacitor of 20 pF and 10 μF, respectively, and a load resistance R_L of 1 M Ω . Reprinted with permission.⁵⁷ Copyright 2020, IEEE. Transient analysis of (c) NAND and (d) NOR gates measured at $V_{DD} = 1$ V. (e) Oscillation frequency and power consumption of a three-stage ring oscillator based on EDLTs, along with (f) the output signal of the ring oscillator ($V_{DD} = 1$ V). Reprinted with permission.¹⁵⁰ Copyright 2020, IEEE.

Based on top-gate EGTs with the same polymer electrolyte, more complex circuits were developed. Aghassi-Hagmann et al. designed, fabricated, and characterized an inkjet-printed full-wave rectifier using diode-connected EDLTs (Figure 14a).⁵⁷ V_{IN} with an amplitude of 1 V and frequencies of 10 Hz and 1 kHz were utilized for the measurements (Figure 14b). The resulting output voltage at an input frequency of 10 Hz indicated that the rectifier worked properly with only a small voltage loss. As the input frequency increased to 1 kHz, the amplitude of the rectified signal decreased as the transistor started to work in a nonquasi-static mode. Carrier accumulation/depletion processes in the channel failed to follow the applied V_G at high frequencies, a signature of the limited polarization

time (> 1 ms) of the electrolyte. Moreover, due to variations in the printing process, the printed polymer electrolyte thickness also varied significantly, leading to different AC characteristics between devices. Overall, the above circuit could effectively rectify V_{IN} as low as 500 mV, and featured a small voltage loss of 140 mV and a cut-off frequency of 300 Hz at a V_{IN} of 1 V. The authors concluded that the device characteristics are suitable for a variety of energy-harvesting applications.

Other logic gates were also realized with top-gate In_2O_3 EDLTs having polymer electrolyte (PVA : propylene carbonate : $\text{LiClO}_4 = 20:63:7$ in mass).¹⁵⁰ As shown in Figures 14c and d, NAND and NOR gates were assembled based on unipolar n-type inverters. The

voltage output characteristics of these NAND and NOR gates revealed well performing characteristics at a driving voltage under 1 V and exhibit switching frequencies of ~ 1 Hz. In addition, NAND gate ring oscillators were fabricated and started functioning at a V_{DD} of only 0.7 V (Figure 14e). The output signal of the ring oscillator recorded at V_{DD} of 1.0 V is shown in Figure 14f. In between a supply voltage level of 0.7 and 1.5 V, the oscillation frequency rose from 271 Hz to 1.14 kHz, respectively.

3.2.2 Type IV, ion gel electrolytes

Ion gel electrolytes are typically composed of an IL dissolved into a polymer network achieved by crosslinking the polymer component (Figure 2d) using either chemical and physical, preferentially photochemical, methods.³³ Frisbie et al reported the first ion gel dielectric for EGTs in 2007, where poly(styrene-block-ethylene oxide-block-styrene) (PS-PEO-PS) with [BMIM][PF₆] (PS-PEO-PS: [BMIM][PF₆] = 1:9 in weight) were adopted in a TGBC transistor structure. In addition to PS-PEO-PS,¹⁵¹⁻¹⁵⁴ several other block copolymers have also been used in ion gel electrolytes including polystyrene-*b*-poly(ethyl acrylate)-*b*-polystyrene (PS-PEA-PS),⁵⁶ and

poly(styrene-*b*-methyl methacrylate-*b*-styrene) (PS-PMMA-PS) (Figure 12b).^{153, 155-157} Note, there are also ion gels that are composed by an IL in inorganic matrixes, e.g. hexagonal boron nitride (hBN).¹⁵⁸ Ion gel electrolytes can be printed as polymer electrolytes, however, due to the liquid nature of the IL, they typically show higher specific capacitance and shorter polarization time, enabling $>$ kHz switching frequencies.¹⁵⁴ As shown in Figure 15a, thus the Frisbie's group reported aerosol jet-printed array of EDLTs on a flexible polyimide substrate, where Au nanoparticle inks were used as the source and drain electrodes, P3HT as the semiconductor, an ion gel ([EMIM][TFSI] with PS-PMMA-PS) as the gate dielectric (~ 20 $\mu\text{F}/\text{cm}^2$ at 10 Hz), and PEDOT:PSS as the gate electrode (Figure 15b, top panel). The transfer characteristics of these devices demonstrated excellent subthreshold behaviour and an I_{ON}/I_{OFF} ratio of 10^5 (Figure 15b). Printed resistor-loaded (20 k Ω resistor by printing carbon ink) EDLT inverters on plastic (Figure 15c) exhibited good inverter characteristics, in which the output voltage was switched between -1.5 V and 0 V as the input gate voltage was swept. Figure 15c also demonstrates that the output voltage of the printed inverter responded well to a 1 kHz square-wave input voltage signal.

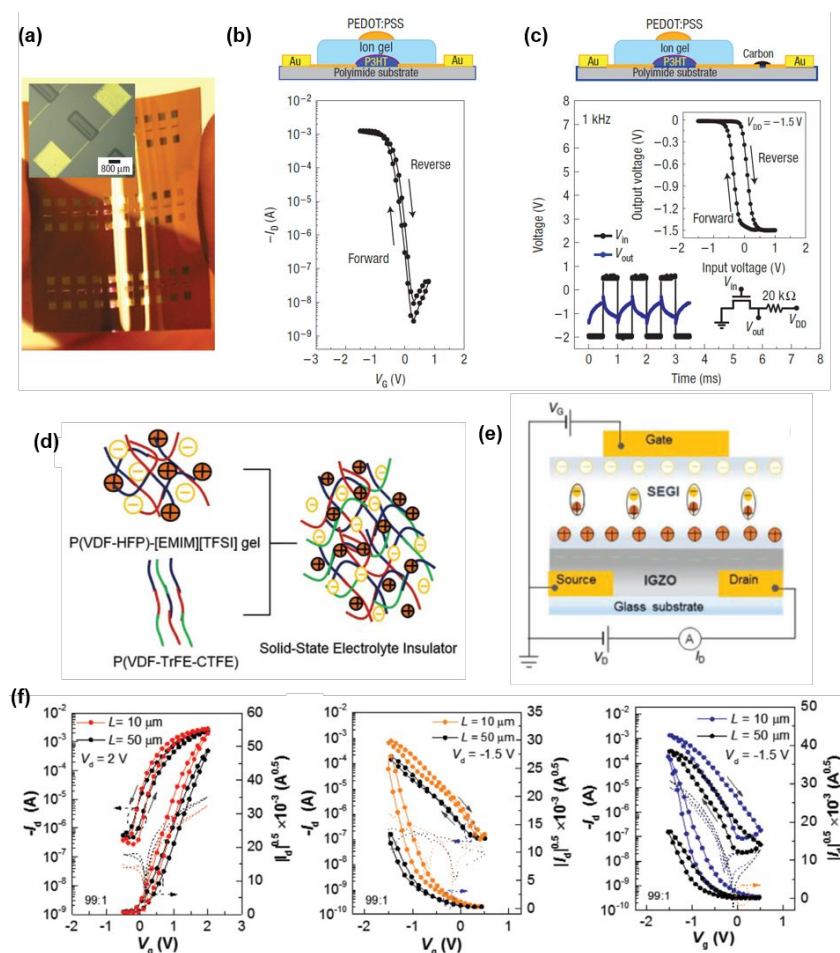


Figure 15. (a) Optical image of an aerosol-printed EDLT array based on an ion gel dielectric (PS-PMMA-PS:[EMIM][TFSI]) fabricated on a flexible polyimide substrate. (b) Transfer characteristic of a P3HT-based EDLT measured at a $V_D = -1$ V ($L = 20$ μm , $W = 1400$ μm). The top of the panel shows the device cross-section schematic diagram. (c) Output voltage response of a resistor loaded EDLT inverter at $V_{DD} = -1.5$ V when V_G is pulsed at 1 kHz. The input–output voltage characteristics are shown in the inset. The top panel shows the device schematic diagram. Reprinted with permission.¹⁵⁴ Copyright 2008, Springer Nature. (d) Schematic representation of the ion gel electrolyte preparation process using P(VDF-HFP):[EMIM][TFSI]+P(VDF-TrFE-CTFE). (e) Cross-sectional diagram of a top-gate/bottom-contact IGZO EDLT. (f) Transfer curves of IGZO,

P3HT and PDFDT based EDLTs. Solid lines and dashed lines represent I_D and gate current (I_G), respectively. Reprinted with permission.¹⁵⁹ Copyright 2020, John Wiley and Sons.

More recently, fluorinated polymers have also been widely used in ion gel electrolytes with the most prominent poly(vinylidene difluoride) (PVDF),^{55, 160} poly(vinylidene fluoride-co-trifluoroethylene) [P(VDF-TrFE)],¹⁶¹ poly(vinylidene fluoride-co-hexafluoropropylene) [P(VDF-HFP)],¹⁶²⁻¹⁶⁵ and poly(vinylidene fluoride-trifluoroethylene-chlorotrifluoroethylene) [P(VDF-TrFE-CTFE)] (Figure 12e).¹⁵⁹ Due to the high- ϵ_r of the polymer component along with the formation of the EDL, high capacitance along with efficient polarization have been achieved. For instance, Noh et al. investigated ion gel electrolytes based on high- k fluorinated polymers where less than 1% of ILs were added. Unlike ion gel dielectrics with conventional block copolymers, in which the IL is a considerable portion of the total mass (typically > 50% in mass), in these ion gel electrolytes the IL mass content is very small, yet, they can achieve capacitance values higher than $1 \mu\text{F}/\text{cm}^2$. The ion gels reported in this study were fabricated by spin-coating a

mixture of P(VDF-TrFE-CTFE) + P(VDF-HFP)-[EMIM][TFSI] in 2-butanone on different semiconductors, including organic polymer and oxide semiconductors (Figure 15d).¹⁵⁹ The authors reported that by increasing the P(VDF-HFP)-[EMIM][TFSI] to P(VDF-TrFE-CTFE) content, the capacitance increased from $49.12 \text{ nF}/\text{cm}^2$ for neat P(VDF-TrFE-CTFE), to 1.96, 4.50 and $5.53 \mu\text{F}/\text{cm}^2$ for the ion gel with a 0.5, 1.0, and 2 v.% of P(VDF-HFP)-[EMIM][TFSI], due to EDL formation. These electrolytes were found to have a good compatibility with different type of semiconductors (e.g. IGZO, CNT, P3HT, PDFDT) and were incorporated in top-gate bottom-contact EDLT structure reported in Figure 15e. These devices exhibited typical transfer curves for driving voltages as low as 1.5 V, substantial on/off switching behaviour, and low I-V hysteresis (Figure 15f). The resulting carrier mobilities were $11.09 \text{ cm}^2/\text{Vs}$ for IGZO, $1.30 \text{ cm}^2/\text{Vs}$ for P3HT, and $2.42 \text{ cm}^2/\text{Vs}$ for PDFDT devices.

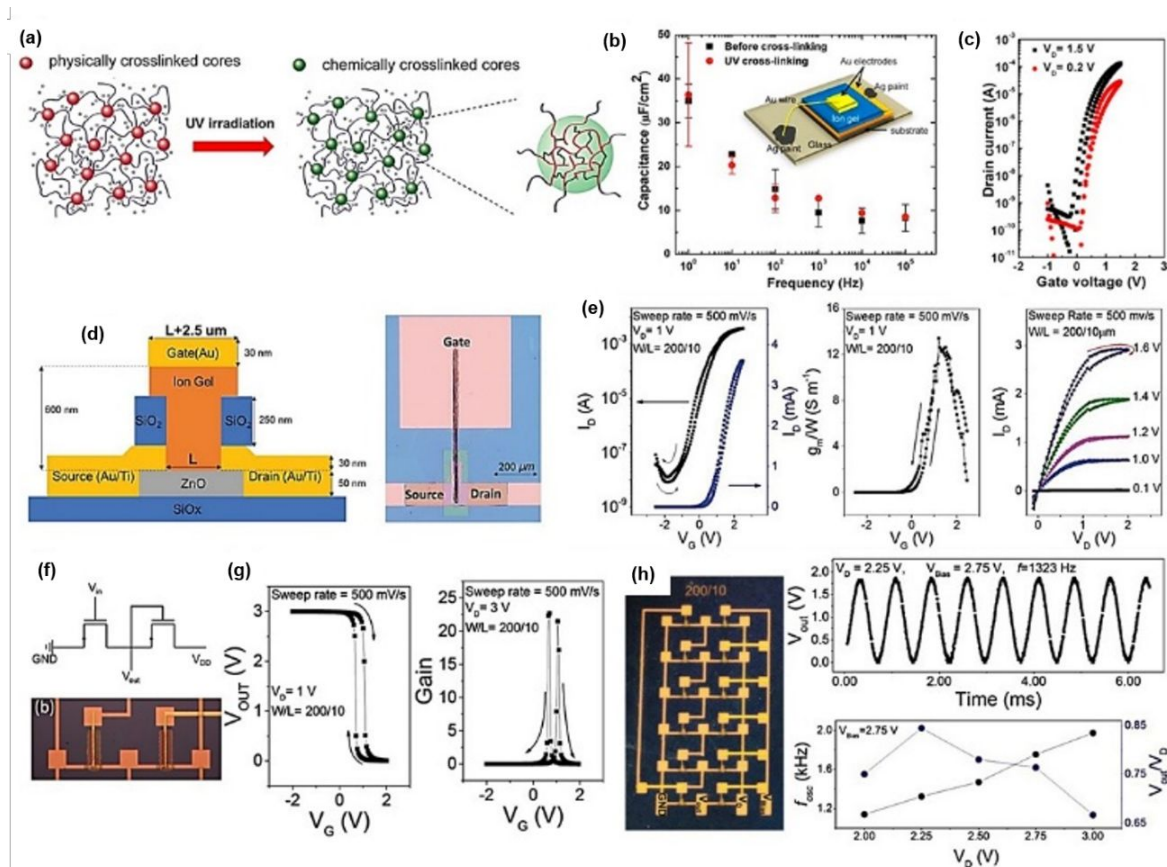


Figure 16. (a) Schematic of chemical cross-linking of SOS-N₃ ion gels by UV irradiation. (b) Frequency dependence of the specific capacitance for SOS-N₃ ion gel films before chemical cross-linking and after UV irradiation for 90 min. The inset shows a schematic of the setup used for measuring the impedance of Au/ion gel/Au capacitor. (c) Transfer characteristics of ZnO EDLTs with photopatterned ion gel. Reprinted with permission.¹⁶⁶ Copyright 2014, American Chemical Society. (d) The device schematic architecture and optical image of a ZnO EDLT with a well patterned ion gel. (e) Transfer curve, channel-width-normalized g_m , and output characteristics of a ZnO EDLT. (f) Scheme and the optical microscope image of an inverter based on ZnO EDLTs, and (g) corresponding quasi-static output versus input and gain measurements at $V_D = 3 \text{ V}$. (h) Optical image of a five-stage ring oscillator based on ZnO EDLTs, and output characteristics of a typical ring oscillator with oscillation frequency as high as 1300 Hz, along with frequency and output range of the ring oscillator as a function of V_D . Reprinted with permission.²¹ Copyright 2019, John Wiley and Sons.

Another important question is whether electrolyte dielectrics can be photopatterned, thus be compatible with conventional photolithographic processes. Frisbie et al. demonstrated a facile

fabrication route to patterned ion gel electrolyte thin films for EGTS using a photo crosslinkable ABA-triblock copolymer.¹⁶⁶ The authors utilized the azide groups of poly(styrene-*r*-vinylbenzylazide) (PS-N₃)

or poly[(styrene-*r*-vinylbenzylazide)-*b*-ethylene oxide-*b*-(styrene-*r*-vinylbenzylazide)] (SOS-N₃, Figure 12d) for photocuring these polymers ($\lambda = 254$ nm) in the presence of the IL [EMIM][TFSI] (Figure 16a). The SOS-N₃ ion gel films were fabricated by a solution-casting (spin-coating or drop-casting) technique from a solution prepared by dissolving SOS-N₃ polymer and [EMIM][TFSI] in ethyl acetate (1:9:10 ratio in weight of SOS-N₃ : [EMIM][TFSI] : ethyl acetate). Interestingly, the authors found that ion transport (ionic conductivity ~ 2 mS/cm) and film microstructure of the ion gel were not affected by UV crosslinking, leading to capacitance greater than ~ 5 $\mu\text{F}/\text{cm}^2$ over the measured frequency range (1–100 kHz) (Figure 16b). N-type (ZnO) EDLTs with a TGBC structure were fabricated and showed a respectable carrier mobility (~ 0.7 cm^2/Vs) and $I_{\text{ON}}/I_{\text{OFF}}$ ratio of $\sim 10^5$ at supply voltages below 2 V (Figure 16c). Recently, the same group further optimized the fabrication process of the EDLTs by utilizing a similar photo crosslinkable polymer (SEAS-N₃, Figure 12d) but screen printing it to carefully control the ion gel overlap with the channel and source/drain electrodes.²¹ These devices consisted of a ZnO semiconductor film deposited by ALD and patterned by photolithography. The Au source and drain electrodes with Ti adhesion layers were then defined by photo lithography followed by deposition of a SiO₂ passivation overlayer, which was deposited by e-beam and patterned by photolithography. Importantly, the SiO₂ passivation layer reduced the contact area of the ion gel with the source and drain electrodes, with the goal of reducing parasitic (also called overlap) capacitance, which can reduce the switching time. The ion gel film, composed of a 1:9 weight ratio mixture of poly(styrene)-*b*-poly(ethylacrylate)-*b*-poly(styrene) triblock copolymer (SEAS, Figure 16d) and [EMIM][TFSI] in ethyl acetate, was screen-printed and UV-crosslinked/patterned. The well-defined 0.5–1 μm thick ion gel films were patterned on the semiconductor channels as a narrow 10 μm stripe. Finally, a stencil was aligned to the gel and used as the mask for the vapor deposition of the Au top gate electrode. Figure 16e reports the quasi-static transfer characteristics at $V_{\text{D}} = 1$ V for a ZnO EDLT exhibiting an electron mobility > 2 cm^2/Vs , $I_{\text{ON}}/I_{\text{OFF}} > 10^5$ and $V_{\text{T}} \sim 0.5$ V. The channel-width-normalized g_{m}/W along with the output characteristics of the device are also shown in Figure 16e, where the linear $I_{\text{D}}-V_{\text{D}}$ traces near $V_{\text{D}} = 0$ V suggests good source/drain contact, along with well-behaving current saturation. The authors also fabricated unipolar inverters (Figure 16f)²¹ exhibiting a gain > 20 from the quasi-static response at $V_{\text{DD}} = 3$ V and a sweep rate of 500 mV/s (Figure 16g). The dynamic performance of the inverter was also investigated and showed a clear response up to 2.5 kHz. A five-stage ring oscillator with an inverter buffer based on the ZnO EDLT inverters was also fabricated (Figure 16h) and exhibited a maximum oscillation frequency of 1.9 kHz at $V_{\text{D}} = 3$ V and $V_{\text{Bias}} = 2.75$ V, which correlated to a stage delay of 50 μs , considering the five-stage ring oscillator rule. The authors concluded that screen printing and photo-crosslinking provided a clean room-compatible method to fabricate EGT circuits with improved sensitivity (gain) and computational power.

It is intuitive that liquid based electrolytes are compatible with mechanical deformation, however, ion gel electrolytes can also

achieve excellent mechanical flexibility/stretchability while preserving dielectric behaviour during stress.¹¹ Lee et al. reported a stretchable EDLT to simulate synapse functions based on organic nanowires consisting of a blend of a diketopyrrolopyrrole conjugated polymer (FT4-DPP) and PEO (7:3, w/w), functioning as the semiconductor, and an ion gel dielectric (PS-PMMA-PS:[EMIM][TFSI] = 0.7:9.3) (Figure 17a).¹⁵⁵ A single nanowire was transferred onto a 100% pre-stretched styrene-ethylene-butylene-styrene (SEBS) rubbery substrate on which CNT source/drain electrodes were patterned. After releasing the strain on the elastic substrate, a wavy nanowire structure was formed, which retained this configuration after repeated stretching to a 100% strain (Figure 17b). The corresponding EDLTs exhibited typical p-type behaviour for driving voltages below 2 V (Figure 17c). The relatively slow formation of the EDLs at the gate/electrolyte and electrolyte/semiconductor interfaces lead to an anticlockwise hysteresis of the transfer characteristics, which could stimulate the behaviour of a biological synaptic response. More importantly, the maximum I_{D} (~ 1 μA) and the carrier mobility remained stable when the EDLT was stretched up to a 100% strain along both the channel length and width directions (Figure 17c) as well as even after 50 cycles at a 100% strain in both directions. The strategy of incorporating a stretchable ion gel dielectric in the EGT is promising for the development of bioinspired soft electronics, neurologically inspired robotics, and electronic prostheses.

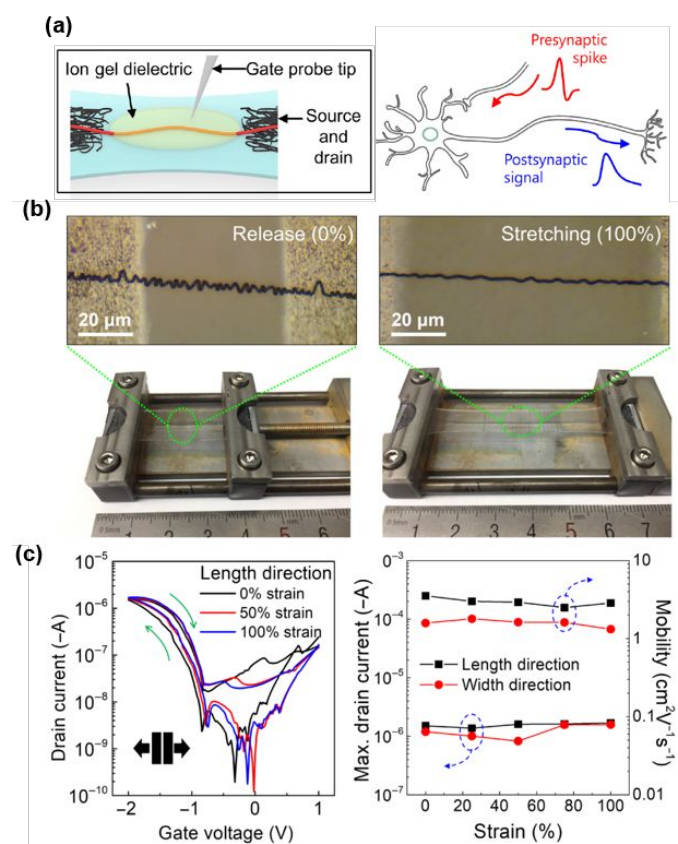


Figure 17. (a) Schematic device structure of an organic nanowire based EDLT and its similarity to the neural signal transmission from preneuron to postneuron through a biological synapse. (b) Optical microscopy image of a wavy nanowire

Review

stretched from 0 to 100% strain. (c) Transfer characteristics of the pre-stretched nanowire based EDLT at 0, 50, and 100% strains, and maximum I_D and mobility as a function of various strains along the channel length and width directions. Reprinted with permission.¹⁵⁵ Copyright 2018, The American Association for the Advancement of Science.

3.2.2 Type V, polyelectrolytes

Polymers containing repeating units bearing an ionic or ionizable group are polyelectrolytes and, depending on the charge type on the polymers, they are classified as polycations and polyanions.^{167, 168} Representative polyelectrolytes used in EGTs are shown in Figure 12e, which include poly(styrene sulfonic acid) (PSSH), with H^+ as counterion;¹⁶⁹ poly(styrene sulfonic acid sodium salt) (PSSNa), with Na^+ as counterion;¹⁷⁰ poly[(vinyl phosphonic acid)-*co*-(acrylic acid)] [P(VPA-AA)], with H^+ as counterion;^{171, 172} poly[(1-vinylpyrrolidone)-*co*-(2-ethyl dimethylammonioethyl methacrylate ethyl sulfate)] [P(VP-EDMAEMAES)], with ethyl sulfate as counterion.¹⁷¹ Some natural polymer derivatives are also common polyelectrolytes used in EGTs, including chitosan,^{74, 173-176} carboxymethyl cellulose and other cellulose derivatives.^{149, 177-179} An efficient way of generating polyelectrolyte is by polymerizing one of the ion of an IL,¹⁸⁰ for example: poly(styrene-*b*-1-[(2-acryloyloxy)-ethyl]-3-butylimidazolium bis(trifluoromethyl sulfonyl)imide-*b*-styrene) (PS-PIL-PS), where TFSI⁻ is the counterion.⁵⁸

As indicated in Section 2, ECTs typically show higher g_m compared to EDLTs, however since the former require bulk ion uptake in the semiconductor, they suffer for slower switching speeds compared with simple EDL formation in EDLTs. The switching speed of a transistor is an important parameter to take into account for the fabrication of circuits operating at high frequencies. Polyelectrolytes are interesting dielectric that can provide fast switching in EGTs, especially for organic polymer based EGTs, since if the redox process occurring in the semiconductor requires the intercalation of the charge located on the immobile polymer component, bulk incorporation is prevented, thus the device can only function as an EDLT.¹⁸¹ In 2007, a pioneer work employed a polyelectrolyte [P(VPA-AA)] as the gate dielectric of P3HT transistors and demonstrated that the electrochemical doping of the *p*-type polymer can be completely prevented, thus these devices functioned as EDLTs.¹⁸² Short switching time (< 0.3 ms) in P3HT based transistor with a top gate structure was realized without patterning of the dielectric and semiconductor, as the electrochemical doping of P3HT bulk was prevented by using only immobile anions in the polyelectrolyte.

Berggren et al. further demonstrated complementary integrated circuits based on organic EDLTs using polyanions and polycations as the gate dielectrics for *p*- and *n*-type transistors, respectively (Figure 18a).¹⁷¹ The polyelectrolytes were matched with the semiconductors to prevent mobile ion penetration in the organic semiconductor, thus as shown in Figure 18a, P(VPA-AA), which conducts H^+ was used to gate the *p*-type poly(2,5-bis(2-thienyl)-3,6-dihexadecylthieno[3,2-*b*]thiophene) (P(T₀T₀TT₁₆)) while P(VP-EDMAEMAES), which conducts ethyl sulfate anions was adopted to gate the *n*-type poly[[N,N'-bis(2-octyl dodecyl)-naphthalene-1,4,5,8-bis(dicarboximide)-2,6-diyl]-alt-

5,5'-(2,2'-bithiophene)] (P(NDI2OD-T2) or N2200). Figures 18b and c show the transfer characteristics of a polyanion and polycation gated transistors, respectively. Both EDLTs show negligible hysteresis indicating that the polyelectrolyte polarizes quickly without significant electrochemical doping of the semiconductor. Moreover, the cut-off frequencies for the *p*- and *n*-type EDLTs in this work were estimated to be 16 kHz and 6.7 kHz, respectively, at a supply voltage of 1 V, which is high considering their electrolyte gating nature. Based on the relatively balanced transistor performances, a complementary inverter was also fabricated (Figure 18d). This circuit showed decent output swings and high gains up to 17.5 for supply voltages between 0.2 V and 1 V. Low static currents of ~ 100 pA at low V_{IN} and ~1 nA at high V_{IN} indicated low power consumption. The authors stressed that it is compatible with portable electronics.

Several natural polyelectrolytes that can be used as electrolyte dielectric have been integrated in EGTs for the realization of artificial synapses, circuits, and sensors.^{172, 179, 183-186} Zhu et al. fabricated chitosan-gated neuromorphic transistor that can work both in EDLT mode and ECT mode depending on the applied V_G (Figure 18e).⁷⁴ Figure 18f shows typical transfer characteristics of the ITO neuromorphic transistor operating as a EDLT, where the I_{ON}/I_{OFF} ratio, SS , V_T , and μ are ~ 1.4×10^6 , 87.1 mV/decade, 0.01 V and 10.7 cm²/Vs, respectively. Here, the applied V_G was not higher than the electrochemical threshold voltage (U_T) of ITO. Note, despite the oxide nature of this semiconductor there are several papers reporting doping and de-doping processes for ITO due to exchange with H^+ .^{183, 187} As shown in Figure 18g, after 1 and 2 V V_G pulses, I_D returns to the initial I_{OFF} value, indicating absence/negligible electrochemical doping of the semiconductor. However, when applying larger (3 and 4 V) V_G pulses, I_D increases to ~38.4 μA and ~53.2 μA , respectively, and when the pulses end (V_G back to 0 V), I_D gradually decays back to ~16.2 μA and ~42.3 μA instead of the initial I_{OFF} value (which were in nA range), signature of an electrochemical process. Figure 18h illustrates the schematic diagram of the operation mechanism of this device. When applying a positive $V_G < 3$ V, protons only accumulate at the chitosan/ITO channel interface, producing an EDL layer. When the gate voltage is above U_T (>3 V), some protons penetrate into the ITO channel, resulting in bulk doping. The doped protons will remain in the ITO channel even when V_G is reset to 0 V, leading to a non-volatile I_D changes which mimics the long-term increase in synaptic weight. Thus, the ITO gate electrode and the ITO channel can be regarded as pre- and post-synaptic signals, respectively (Figure 18e). Consecutive V_G spikes hold the potential to adjust the synaptic weight of the neuromorphic transistor (Figure 18i). By reading out the synaptic weight with a small V_D pulse, the authors showed that positive potentiation voltage spikes (P) incrementally increased the synaptic weight from ~ 4.0 to ~ 11.0 μA (Figure 18j). While negative depression voltage spikes (D) incrementally decreased the synaptic weight from ~ 11.0 to ~ 4.0 μA . Furthermore, good repeatability of this modulation was confirmed through six P/D cycles. This result demonstrated potential applications of the proposed oxide neuromorphic transistors in flexible neuromorphic cognitive platforms.

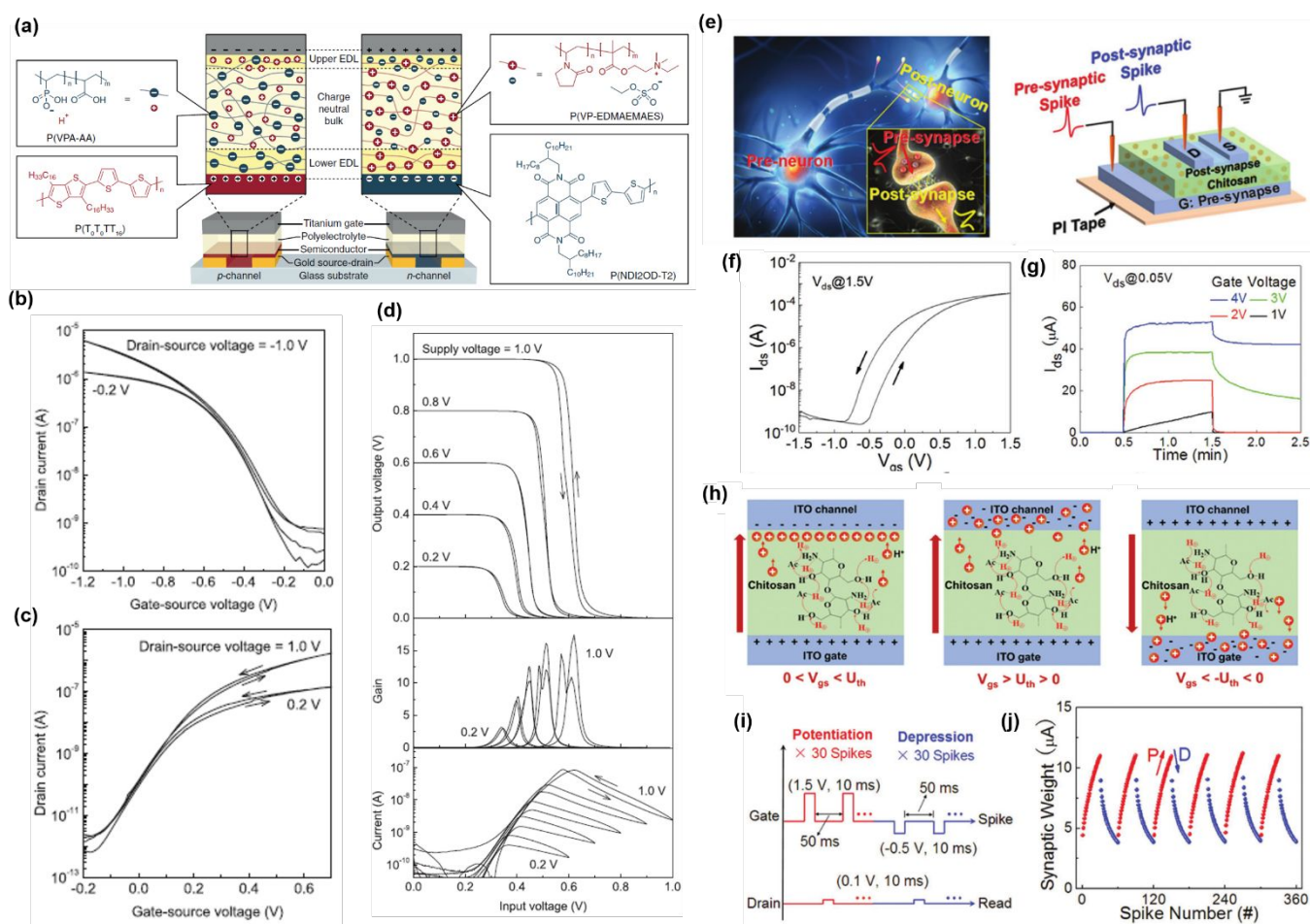


Figure 18. (a) Materials used for fabricating complementary polyelectrolyte-gated EDLTs. Schematic cross sections and illustrations of the charge distribution within the polyelectrolyte gate insulator layers in *p*- and *n*-channel transistors that are gated with negative and positive gate voltages, respectively. Transfer characteristics for (b) a *p*-type EDLT with a P(VPA-AA) dielectric, and for (c) an *n*-type EDLT with a P(VP-EDMAEMAES) dielectric. (d) Complementary polyelectrolyte-gated inverter performance based on *p*- and *n*-type EDLTs. Reprinted with permission.¹⁷¹ Copyright 2011, John Wiley and Sons. (e) Schematic illustration of a biological synapse, and a chitosan gated ITO neuromorphic transistor. (f) Transfer curves of an ITO neuromorphic transistor, and (g) I_D triggered by gate pulses with different amplitudes at a constant duration of 1 min. (h) Operation mechanism for an ITO neuromorphic transistor operated under different gate bias. (i) Schematic diagram of the spike trains. Thirty consecutive potentiation (P) gate spikes are followed by 30 consecutive depression (D) gate spikes. (j) Obtained synaptic weights after receiving consecutive P and D spikes. Reprinted with permission.⁷⁴ Copyright 2018, John Wiley and Sons.

3.3 Type VI, oxide electrolytes

Oxide electrolytes have been extensively investigated in the area of batteries and fuel cells for the realization of more reliable and safer energy conversion and storage devices.^{41, 42} However, these materials have been rarely reported as gate dielectrics of transistors particularly due to relatively complex fabrication process and lack of in-depth understanding on the electrolyte gating phenomenon in some solution processed oxide dielectrics, for instance, H rich AlO_x (*vide infra*).^{188, 189}

Katz et al. pioneered the use of sodium beta-alumina (SBA) dielectric for fabricating both metal oxide and organic EDLTs.^{60, 190} SBA film was prepared by spin-coating a the SBA precursor sol, consisting of sodium acetate and $\text{Al}(\text{OC}_4\text{H}_9)_3$ in water, on ITO glass or Si wafer substrates followed by thermal annealing up to 830 °C. Next, the semiconductor and the source/drain electrodes were then deposited to form an EDLT with a BGTC structure. SBA is an excellent

high capacitance electrolyte due the unique multilayer structure having mobile Na^+ within the AlO_x lattice planes but negligible ionic and electronic interlayer charge transport (Figure 19a). C-F measurements were carried out on metal-insulator-metal structures and SBA films exhibited a capacitance of 2.0 $\mu\text{F}/\text{cm}^2$ at 50 Hz, which is much greater than that of typical inorganic oxide dielectric films. The capacitance of the SBA film decreased with frequency, which was expected due to the limited ion polarization time (Figure 19b). However, a high capacitance of 350 nF/ cm^2 was also measured at 1 MHz, which implied that high-frequency/low-voltage operation EDLTs could be realized. Figure 19c shows the transfer characteristic of a BGTC zin-tin-oxide (ZTO) EDLT based on SBA operating at $V_D = 2$ V in an ambient atmosphere. This device showed an $I_{\text{ON}}/I_{\text{OFF}}$ ratio of 2×10^4 and negligible hysteresis. Moreover, the calculated average effective mobility was in the range of 22 - 29 cm^2/Vs , assuming a '1 Hz-frequency' extrapolated capacitance of 2.5 $\mu\text{F}/\text{cm}^2$.

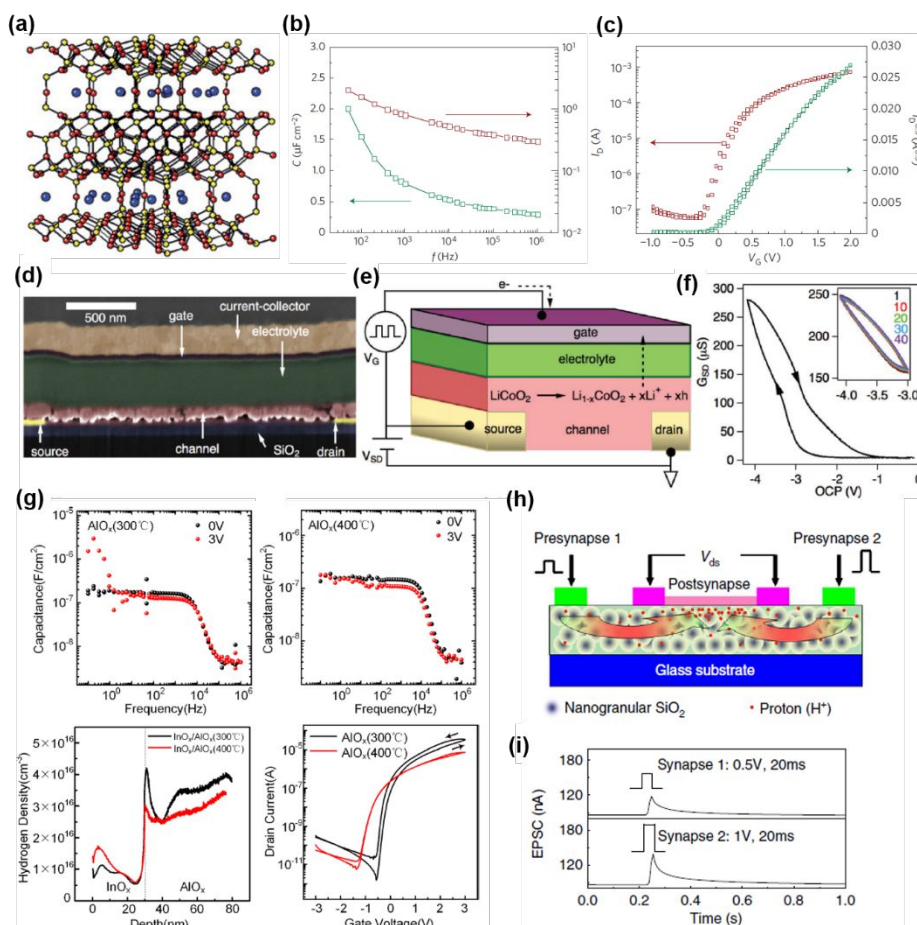


Figure 19. (a) Crystal structure of sodium beta-alumina (SBA), where blue represents the mobile sodium ions and red and yellow represent oxygen and aluminum atoms, respectively. (b) C-F characteristics of a 75nm SBA film. (c) Transfer characteristics for a ZTO transistor fabricated on ITO glass substrate with SBA as dielectric. Reprinted with permission.⁶⁰ Copyright 2009, Springer Nature. (d) False color cross section SEM image showing the device structure of a Li-ion synaptic transistor. (e) Schematic of the synaptic transistor with $\text{Li}_{1-x}\text{CoO}_2$ as channel material and LiPON as electrolyte. (f) Source-drain conductance (G_{SD}) as a function of V_G , with V_D of 100 mV. The inset shows repeated cycling over the voltage window of -4.1 V < OCP < -3.0 V. The cycle numbers 1, 10, 20, 30, and 40 are shown in various colors. Reprinted with permission.¹⁹¹ Copyright 2017, John Wiley and Sons. (g) C-F characteristics of AlO_x dielectric films annealed at 300 °C and 400 °C, with the secondary ion mass spectrometry (SIMS) hydrogen depth profiles of $\text{AlO}_x/\text{InO}_x$ stacking layers, and the transfer curves of the $\text{AlO}_x/\text{InO}_x$ transistors in the saturation region. Reprinted with permission.¹⁹² Copyright 2020, AIP Publishing. (h) Schematic image of the laterally coupled synaptic transistor with two in-plane gates based on nanogranular SiO_2 electrolytes. (i) Excitatory postsynaptic currents (EPSCs) triggered by presynaptic spike 1 (0.5 V, 20 ms) and presynaptic spike 2 (1.0 V, 20 ms), respectively. Reprinted with permission.¹⁹³ Copyright 2014, Springer Nature.

Another interesting approach to fabricate an ECT with an oxide electrolyte is to convert a well-developed Li-ion battery (LIB), a two terminal device, to a transistor, by defining the source/drain electrodes and transistor channel at the anode (cathode) side of the battery, while the cathode (anode) side acts as the gate electrode.^{191, 194} An example of this approach is shown in Figure 19d, where the authors fabricated a Li-ion synaptic transistor (LISTA) using a Pt source and drain electrodes (yellow) contacting a 120 nm thick $\text{Li}_{1-x}\text{CoO}_2$ channel (red) with channel length of 2 μm . A 400 nm thick lithium phosphorous oxynitride electrolyte (LiPON) layer (green) separated the channel from a 50 nm Si gate electrode (purple). The LiPON solid electrolyte was chosen for the large chemical stability window and high electrical resistivity ($>10^{15} \Omega\text{cm}$).¹⁹⁵ This EGT worked as an ECT due to the bulk (de)doping of Li ion in $\text{Li}_{1-x}\text{CoO}_2$ channel. Figure 19e illustrates the resistance switching mechanism in this LISTA device. Here, V_G determines the source–drain conductance, G_{SD} , by controlling the Li content in the channel.

Application of a negative V_G to the open circuit potential (OCP = V_G at $I_{GD} = 0$ A) electrochemically drives Li-ions from the channel into the gate electrode through the solid electrolyte. For $\text{Li}_{1-x}\text{CoO}_2$, the removal of Li oxidizes Co from +3 to +4 and generates positively charged polarons. As the fraction x in $\text{Li}_{1-x}\text{CoO}_2$ varied from 0 to 0.5 the electronic conductivity increased by nearly six orders of magnitude. This process is highly reversible as proved in well-developed rechargeable LIB, and a positive V_G with respect to OCP re-intercalates Li ions in $\text{Li}_{1-x}\text{CoO}_2$ and the channel becomes insulating again (Figure 19f).

Other than conventional oxide electrolyte typically used in batteries, other oxides, including amorphous Li doped and H doped/rich AlO_x are also emerging as solid electrolytes that can provide superior dielectric performance.^{50, 196, 197} Note, even though for conventional AlO_x dielectric, the mobile hydrogen would lead to an overestimation of carrier mobility, large hysteresis, and performance instability, this property can be extremely useful for

applications of memristors and artificial synapses.^{188, 189} Pei et al. proposed transistor-based artificial synapses that were simply constructed with a solution-processed InO_x channel and an AlO_x electrolyte gate dielectric.¹⁹² Due to the mobile hydrogen in low temperature processed AlO_x (Figure 19g), under a positive gate bias, the hydrogen can either form an EDL or electrochemically dope InO_x , depending on the magnitude of V_G , leading to short term potentiation or long term potentiation. Synapse based on this all-oxide structure typically showed much more stable performance when compared to other artificial synapses based on EGT with IL or aqueous solution electrolytes.

Nanogranular SiO_2 can also be an efficient proton conductor and was integrated in an in-plane lateral-coupled oxide-based artificial synapse network based on EDLTs with multiple side-gates.^{43, 193, 198, 199} Multiple pre-synapses were recorded in this lateral structure due to the proton-related EDL effect (Figure 19h). When a presynaptic spike was applied on the pre-synapse (a V_G pulse on the side-gate electrode), protons migrated to the SiO_2/IZO interface and triggered an excitatory postsynaptic current (EPSC). A presynaptic spike (0.5 V, 20 ms) applied on presynapse 1 would trigger an EPSC 1 with an amplitude of ~ 30 nA and a presynaptic spike (1.0 V, 20 ms) applied on pre-synapse 2 would trigger an EPSC 2 with an amplitude of ~ 50 nA (Figure 19i). When two presynaptic spikes were applied on presynapse 1 and presynapse 2, protons migrated to the interface region accumulated, therefore the two EPSCs would be summed in the postsynapse. Such summation is a dynamic analogue function of time. These results demonstrated that the spatiotemporal EPSC summation in this laterally coupled synaptic transistor can effectively simulate spatiotemporally correlated signal processing.

3.4. Electrolyte dielectric in series

The six types of electrolyte dielectrics exhibit advantages and disadvantages. By utilizing two or more types of electrolyte dielectrics simultaneously, or employing electrolyte dielectrics in series, could hold great potentials to maximize advantages. For instance, proper function of sensor devices requires high selectivity along with good sensitivity. While EGT based sensors have demonstrated extraordinary sensitivities, they typically show no or inferior selectivity when adopting a single type of electrolyte.²⁰⁰ Moreover, most the EGT sensors were based solely on aqueous electrolyte, which is an issues for long-term stability due to water evaporation. To enable good selectivity and stability, more than one type of electrolyte have been utilized with one EGT to balance selectivity and stability.^{200, 201} A representative device structure of this type is shown in Figure 20a.²⁰² This OECT used a PEDOT:PSS channel on which a glass ring chamber was mounted and filled with a agarose aqueous solution (1 wt.%), KCl (10^{-3} M), and disodium ethylenediamine tetraacetic acid (Na_2EDTA , 5×10^{-2} M). After gelation of the electrolyte at room temperature, the chamber was sealed by placing a standard PVC-based K^+ -selective membrane on top of the hydrogel. Finally, a top rubber chamber (2 mL volume) was used for

containing the analyte solution and the gate electrode (Ag/AgCl). This kind of device should show specific selectivity to K^+ , and the selectivity can be easily tuned by just changing the ion selective membrane. For instance, by using a Na^+ -selective membrane, a highly sensitive and selective Na^+ OECT sensor is achieved.²⁰¹ As shown in Figure 20b, I_D was recorded at a constant V_G and V_D while the Na^+ concentration in the water (analyte) was increased stepwise. The Na^+ concentration was adjusted by adding a certain amount of different saline solutions (10^{-4} – 10^{-1} M NaCl) to a larger reservoir (here a 200 mL H_2O beaker) which was connected via PVC tubing to the flow cell and further to retracing micro syringes, producing a constant flow of 1 ml/min. An extremely sensitive response on I_D (decrease of ~ 250 – 500 nA/dec) was observed by varying the Na^+ concentration from 10^{-6} M to 10^{-1} M due to the change in effective gate potential. Furthermore, good reversibility and selectivity of this ion-sensitive OECT was demonstrated (Figure 20c). Fast response towards Na^+ was observed when the concentration was varied between 10^{-4} M Na^+ (base line) and 10^{-3} M Na^+ , while a weak response ($\sim 7\%$ on the variation of I_D) to high concentration K^+ (10^{-2} M) is observed. In comparison, by only increasing from 10^{-4} M to 10^{-3} M Na^+ , 5 times higher I_D change was detected, confirming the superior selectivity to Na^+ ions.

Several newly developed semiconducting polymers exhibit superior electrochemical doping capabilities, however, they are poor ionic conductors of biologically relevant ions (K^+ , Na^+ , Cl^- et al).^{32, 73} Ginger et al. changed the transistor operating mode from that of an organic EDLT to that of an OECT by incorporating an ion exchange gel dielectric between the semiconducting polymer layer and the aqueous electrolyte dielectric (Figure 20d).²⁰³ The ion exchange gel in this device is composed of a blend of (PVDF-HFP) and [BMIM][TFSI]. [BMIM][TFSI] and was chosen as the IL component because it is immiscible with water and contains TFSI^- , an anion that efficiently diffuses and dopes hydrophobic conjugated polymers. The semiconducting polymer is poly[2,5-bis(3-tetradecylthiophen-2-yl)thieno[3,2-b]thiophene] (PBTTT) and was selected because of the high FET mobility (~ 1.0 cm^2/Vs), yet this polymer is very textured and hydrophobic and is unable to uptake biologically relevant anions in the absence of the ion exchange gel. The device working principle is that upon application of a V_G , Cl^- ions from the aqueous electrolyte enter the ion exchange gel and TFSI^- ions enter the underlying semiconductor polymer active layer, compensating for holes on the polymer backbone (Figure 20d). Figure 20e shows the transfer curves of OECTs with and without the ion gel. The transfer curve shows greatly enhanced I_D when employing ion gel, which is more than four orders of magnitude compared to that in device without ion gel. The g_m increases from $\sim 1.0 \times 10^{-4}$ to ~ 9.0 mS upon applying the ion exchange gel, along with enhanced $I_{\text{ON}}/I_{\text{OFF}}$ ratio from ~ 4.4 to 10^5 . Figure 20f shows the corresponding output curves with the ion exchange gel applied, which show decent linear and saturation regimes.

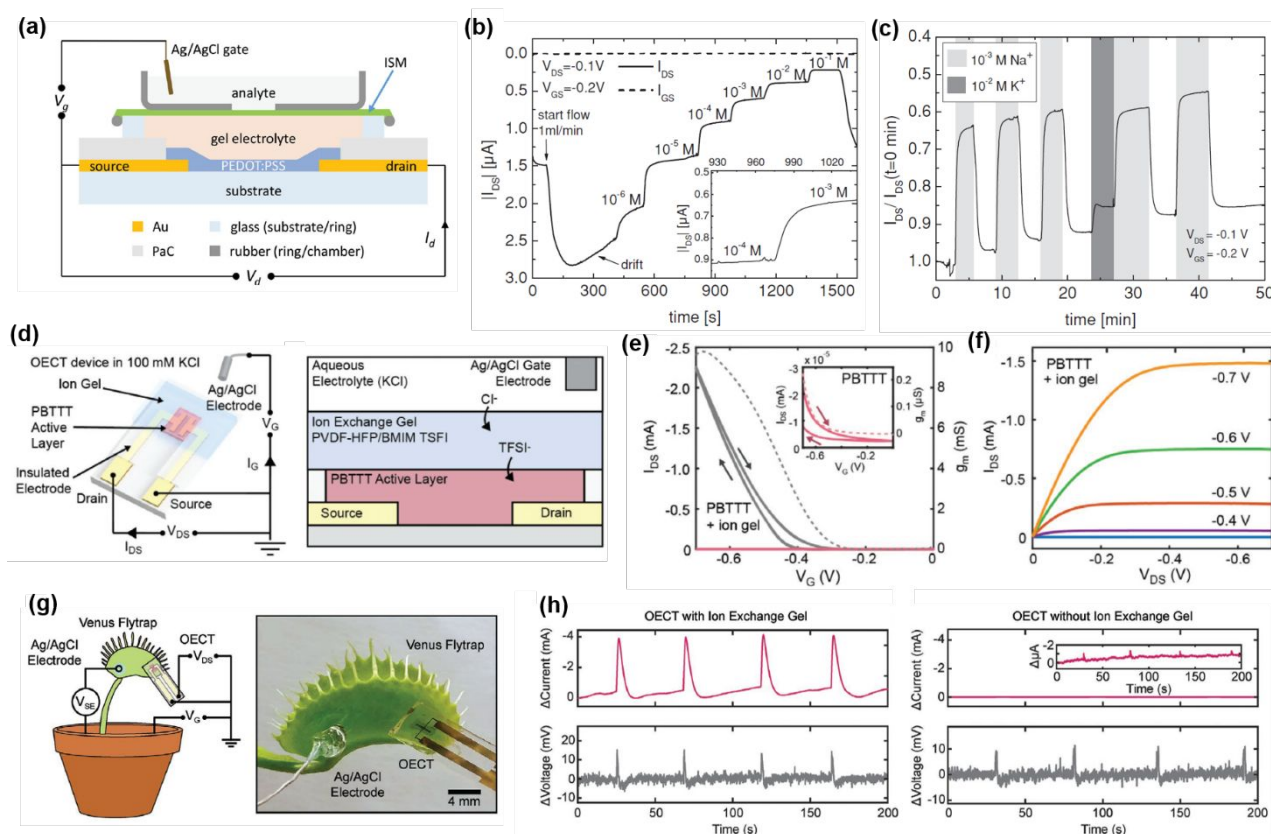


Figure 20. (a) Cross section schematic of the ion sensitive OECT. Reprinted with permission.²⁰² Copyright 2014, John Wiley and Sons. (b) I_D response to an increasing Na^+ concentration of a typical ion-sensitive OECT with a PVC ion-selective membrane, exhibiting a response time of ~ 30 s (see inset). (c) Response curve of a Na^+ selective OECT. Reprinted with permission.²⁰¹ Copyright 2013, John Wiley and Sons. (d) OECT device schematic with the ion exchange gel positioned on top of the active layer, along with the schematic of OECT operation upon application of a gate bias, ions from solution (Cl^-) enter the ion exchange gel and ions from the ion exchange gel (TFSI^-) enter and dope the semiconductor polymer layer. (e) Transfer curve of the OECT with and without the ion exchange gel and g_m as a function of V_G (dotted line). The inset shows the transfer curve and g_m as a function of V_G (dotted line) of the OECT without the ion exchange gel. (f) Output curves for the OECT with the ion exchange gel. (g) Schematic of the standard Ag/AgCl electrode and ion exchange gel based OECT attached to a Venus flytrap. (h) Current and voltage as a function of time from an OECT and an Ag/AgCl electrode, respectively, upon triggering the hair inside the flytrap four times. Reprinted with permission.²⁰³ Copyright 2020, John Wiley and Sons.

Next, as a practical demonstration, ion-exchange-gel-modified OECTs were used for measuring extracellular action potentials of a Venus flytrap (*Dionaea muscipula*) upon mechanical stimulation. The upper leaf of the Venus flytrap typically contains six trigger hairs, which generate an action potential when stimulated. A commercial Ag/AgCl electrode wire and an OECT with ion exchange gel on the surface of the Venus flytrap leaf were placed on the leaf of the Venus flytrap and the signals from both the OECT and Ag/AgCl electrodes were simultaneously recorded while stimulating the hairs to activate the action potential (Figure 20g). Note, an aqueous 0.1 M KCl solution was used to interface with the plant and the ion exchange gel. As the stimulation on trigger hair was applied, traces of I_D /voltage versus time showed the simultaneous recording of the action potential on both the ion exchange gel based OECT and a standard commercial Ag/AgCl wire electrode (Figure 20h, left). The Ag/AgCl electrode served as a control and measured changes in potential between the Venus flytrap leaf and ground. The signal-to-noise ratio (SNR) by dividing the amplitude of the depolarization peak (I_A or V_A) by the standard deviation (σ) of the noise without flytrap stimulation were calculated. SNR increased from ~ 10 ($I_A = \sim 0.27 \mu\text{A}$, $\sigma = 28$ nA) to ~ 1250 ($I_A = 35 \mu\text{A}$, $\sigma = 28$ nA) when the ion exchange

gel was applied. These results showed the possibility of using interface engineering to open up a wider palette of organic semiconductors as OECTs that can be gated by aqueous solutions.

4. Summary and Perspective

In conclusion, we reviewed the major electrolyte materials used in EGTs with details of their chemical structures/properties, electronic/ion performances, and particularly emphasized their impact on EGT function and field of use in different applications.

To better compare the different Types of electrolyte in this summary section, Table 1 compiles major dielectric properties including specific capacitance, thickness, cut-off frequency, highest applied voltage, and working temperature. All of the electrolytes show high capacitance, typically higher than $1 \mu\text{F}/\text{cm}^2$; although in some studies capacitances higher than $1000 \mu\text{F}/\text{cm}^2$ for electrolytes based on Types I, II, or V have been reported due to the bulk doping in ECTs. Except for Type I and II electrolytes, the thickness of the other classes can be controlled to be under 100 nm, where thicknesses as low as 20 nm are reported in oxide electrolytes.¹⁹⁷ On the other hand, since the formation of the EDL is minimally affected

by the electrolyte thickness, thick electrolyte films of more than 500 μm can also be utilized. However, as mentioned in Section 2.1, thicker dielectrics will definitely increase the switching times and reduce operating frequencies. Consequently, for Types I and II electrolytes, cut-off frequencies are typically lower than 10^3 Hz, while by optimizing the thickness of other solid-state electrolytes, cut-off frequencies can be enhanced to as high as 10^6 Hz. Furthermore, the highest applied voltage and working temperature are the two parameters that primarily limit the applications of different types of electrolytes, where Type I electrolytes have the narrowest voltage and temperature ranges, while Type VI electrolytes are more robust, having broad applicability over broader voltage and temperature ranges.

Table 1. Summary of the dielectric properties of different types of electrolytes.

Electrolyte dielectric	C ($\mu\text{F}/\text{cm}^2$)	d (μm)	Cut-off frequency (Hz)	Highest applied voltage (V)	Working temperature ($^\circ\text{C}$)
Type I: Aqueous solutions	1 - 10000	NA	$< 10^3$	~ 1	< 100
Type II: Ionic liquids	2 - 2000	NA	$< 10^4$	~ 3	< 400
Type III: Polymer electrolytes	1 - 100	0.1 - 500	$< 10^3$	~ 3	< 300
Type IV: Ion gels	1 - 200	0.05 - 400	$< 10^6$	~ 3	< 300
Type V: Polyelectrolytes	0.2 - 3000	0.05 - 100	$< 10^4$	~ 3	< 300
Type VI: Oxide electrolytes	0.5 - 1.6	0.02 - 1	$< 10^4$	Can be > 5 V	< 700

Considering the different dielectric properties of these materials, they are more or less differently suited for certain applications. However, all these types of electrolytes can all be used for synaptic simulation, as the key synaptic feature is based on the relatively slow polarization of the electrolyte component. Except for Type VI electrolytes (oxides), all other electrolytes should be equally suitable for flexible/stretchable electronics. Note, Type VI electrolytes can also be used for flexible electronics, but would typically exhibit less reliable mechanical properties than the other electrolytes. Type I electrolytes are best suited for bio-interfacing and biosensing purposes due to its biocompatibility, while they are less reliable for circuit integration compared to solid-state electrolytes (Types III - VI). Nevertheless, research highlights in human-machine interfacing and brain-computer interfacing may further facilitate the development of circuits based on Type I electrolytes. Studies on liquid-based electrolytes provided important insights on how different ions affect EGT performance. Moreover, since the majority of polymer-based electrolytes rely on the same (or at least one of them for polyelectrolytes) mobile ions used in liquid-based electrolytes to

form the EDL, the development and mechanistic insights for liquid-based electrolytes facilitated the development of polymer-based electrolytes. For example, it was found that the ionic liquid [EMIM][TFSI] is compatible with most of the semiconductors used in EGTs, thus several studies on ion gel electrolytes incorporated [EMIM][TFSI] to fabricate high performance EGTs.^{160, 166, 204} Furthermore, ion impacting the functionality and performance of p-type OECT have been widely investigated, thus the anions affording efficient/fast electrochemical doping of p-type polymers have been identified and are now widely used.^{73, 97, 98, 205} However, the development of high-performance n-type OECTs remains far behind their p-type counterparts. This is partially due to design and synthesis challenges of high-performance n-type electrochemically active polymers. Thus, greater investigation and deeper understanding of how the electrolyte affects n-type polymer durability and performance may provide additional insight to new electron-conducting polymer design/synthesis. Importantly, identification of optimal electrolytes, and particularly the cationic component, for n-type OECTs should not only be limited to ion pairing, cation penetration, solvent-induced active layer swelling effects, but also involve understanding of suppression of side reactions during application of the positive bias, which can be more detrimental for negative vs. positive (bi)polaronic species. Moreover, since aqueous-based electrolyte are widely used in bio-related applications, such as physiological sensing, which directly use biological fluids as the electrolyte, the stability of the electrolytes under bias need to be studied more accurately, as any side reaction and overshoot of the bias voltage (considering the electrochemical window of aqueous electrolytes is only ~ 1 V) could lead to toxic byproduct generation.

The development of printed circuits based on EGTs have accelerated with the incorporation of polymer-based electrolytes and various logic gates. For instance, ring oscillators can now operate at frequencies of more than 10 kHz.⁵⁶ However, their commercialization will require well-defined patterning of all EGT components including the electrolyte, which can further enhance the operation frequency and minimize the overall power consumption by decreasing parasitic capacitive effects. The development of more efficient photopatternable polymer-based electrolytes is thus of primary importance for applications and could be an effective way to accelerate introduction of this technology as well as reducing fabrication costs. Pioneer works have proven the feasibility of this approach,²¹ but patterning efficiency and resolution need further improvements. Furthermore, for certain applications it is essential that the process is compatible with existing conventional semiconductor FAB manufacturing techniques.

The thermal stability and the maximum operating voltage of electrolyte dielectrics are much more limited compared to conventional dielectrics, preventing EGT application in several areas where large operating temperature and/or voltages are required for device function such as in bionic robotics, smart textiles, and electrophoretic displays. Oxide electrolytes exhibit far better thermal stability and can sustain far larger break-down voltages/electric

Review

fields than other type of electrolytes, and they may enable EGTs for these applications. While most of the high-performance oxide electrolytes still require far higher processing temperatures compared to liquid and polymer-based electrolytes, there are promising new approaches to fabricate them at temperature compatible with plastic substrates. Finally, EGT operating speeds are too low for applications in, eg, video rate displays. However, there is a large space where far slower imaging processing are required, e.g., in electronic shelf label and ultra-large/low resolution signage, and this could be important fields where new and exciting electrolyte/EGT research can occur.

Overall, the development of EGTs relies on research progress in both semiconductors and electrolytes. Since most of the EGT research to date has focused on semiconductors, equally important challenges and thus opportunities lie with the electrolyte. A lot can be learned from fields where electrolytes have been actively pursued such as batteries, supercapacitors, fuel cells, drug delivery, catalysis, actuators, dye sensitized solar cells, and electrochromic devices. Thus, active collaborations between the transistor community with other research and technological areas should afford significant advances, considering the similarity in several aspects of processability, ionic conductivity, and stability. We believe the progress in electrolyte materials will greatly influence the development of EGTs, and represents one of the barriers for the large-scale commercialization of EGT-based devices.

Conflicts of interest

There are no conflicts to declare.

Acknowledgements

The authors gratefully acknowledge financial support by AFOSR grant FA9550-18-1-0320, Northwestern University MRSEC grant NSF DMR-1720139, U.S. Department of Commerce, National Institute of Standards and Technology as part of the Center for Hierarchical Materials Design (CHiMaD) award 70NANB19H005, National Natural Science Foundation of China (No. U1830207) and Flexterra Corp.

Notes and references

1. K. Sim, Z. Rao, F. Ershad and C. Yu, *Adv. Mater.*, 2020, **32**, e1902417.
2. J. H. Koo, J. K. Song, S. Yoo, S. H. Sunwoo, D. Son and D. H. Kim, *Adv. Mater. Technol.*, 2020, **5**, 2000407.
3. X. Xu, S. Xie, Y. Zhang and H. Peng, *Angew. Chem. Int. Ed. Engl.*, 2019, **58**, 13643-13653.
4. D. Ji, T. Li and H. Fuchs, *Nano Today*, 2020, **31**, 100843.
5. 'Better Yield on 5nm than 7nm': TSMC Update on Defect Rates for N5, www.anandtech.com, (accessed June, 2021).
6. S. B. Desai, S. R. Madhvapathy, A. B. Sachid, J. P. Llinas, Q. Wang, G. H. Ahn, G. Pitner, M. J. Kim, J. Bokor, C. Hu, H. P. Wong and A. Javey, *Science*, 2016, **354**, 99-102.
7. D. Ji, J. Jang, J. H. Park, D. Kim, Y. S. Rim, D. K. Hwang and Y. Y. Noh, *J. Inf. Disp.*, 2020, **22**, 1-11.
8. U. Zschieschang and H. Klauk, *J. Mater. Chem. C*, 2019, **7**, 5522-5533.
9. V. Milo, G. Malavena, C. Monzio Compagnoni and D. Ielmini, *Materials*, 2020, **13**, 166.
10. T. Someya, Z. Bao and G. G. Malliaras, *Nature*, 2016, **540**, 379-385.
11. H. Wang, Z. Wang, J. Yang, C. Xu, Q. Zhang and Z. Peng, *Macromol. Rapid Commun.*, 2018, **39**, 1800246.
12. J. Borges-González, C. J. Kousseff and C. B. Nielsen, *J. Mater. Chem. C*, 2019, **7**, 1111-1130.
13. V. G. Reynolds, S. Oh, R. Xie and M. L. Chabiny, *J. Mater. Chem. C*, 2020, **8**, 9276-9285.
14. H. Sun, J. Gerasimov, M. Berggren and S. Fabiano, *J. Mater. Chem. C*, 2018, **6**, 11778-11784.
15. W. H. Brattain and C. G. B. Garrett, *Bell Syst. Tech. J.*, 1955, **34**, 129-176.
16. S. T. Keene, C. Lubrano, S. Kazemzadeh, A. Melianas, Y. Tuchman, G. Polino, P. Scognamiglio, L. Cina, A. Salleo, Y. van de Burgt and F. Santoro, *Nat. Mater.*, 2020, **19**, 969-973.
17. H. W. Du, X. Lin, Z. M. Xu and D. W. Chu, *J. Mater. Sci.*, 2015, **50**, 5641-5673.
18. J. C. Dutta, presented in part at the 2012 2nd National Conference on Computational Intelligence and Signal Processing (CISP), 2012.
19. T. G. Backlund, H. G. O. Sandberg, R. Osterbacka and H. Stubb, *Appl. Phys. Lett.*, 2004, **85**, 3887-3889.
20. M. S. Chae, J. H. Park, H. W. Son, K. S. Hwang and T. G. Kim, *Sens. Actuators, B*, 2018, **262**, 876-883.
21. F. Zare Bidoky, B. Tang, R. Ma, K. S. Jochem, W. J. Hyun, D. Song, S. J. Koester, T. P. Lodge and C. D. Frisbie, *Adv. Funct. Mater.*, 2019, **30**, 1902028.
22. J. T. Yang, C. Ge, J. Y. Du, H. Y. Huang, M. He, C. Wang, H. B. Lu, G. Z. Yang and K. J. Jin, *Adv. Mater.*, 2018, **30**, 1801548.
23. S. Park, S. Lee, C. H. Kim, I. Lee, W. J. Lee, S. Kim, B. G. Lee, J. H. Jang and M. H. Yoon, *Sci. Rep.*, 2015, **5**, 13088.
24. S. M. Kim, C. H. Kim, Y. Kim, N. Kim, W. J. Lee, E. H. Lee, D. Kim, S. Park, K. Lee, J. Rivnay and M. H. Yoon, *Nat. Commun.*, 2018, **9**, 3858.
25. H. Shimotani, T. Kanbara, Y. Iwasa, K. Tsukagoshi, Y. Aoyagi and H. Kataura, *Appl. Phys. Lett.*, 2006, **88**, 073104.
26. P. Gkoupidenis, N. Schaefer, B. Garlan and G. G. Malliaras, *Adv. Mater.*, 2015, **27**, 7176-7180.
27. H. Xu, S. Fathipour, E. W. Kinder, A. C. Seabaugh and S. K. Fullerton-Shirey, *ACS Nano*, 2015, **9**, 4900-4910.
28. J. Chung, A. Khot, B. M. Savoie and B. W. Boudouris, *ACS Macro Lett.*, 2020, **9**, 646-655.
29. E. Zeglio and O. Ingnas, *Adv. Mater.*, 2018, **30**, 1800941.
30. L. Kergoat, B. Piro, M. Berggren, G. Horowitz and M. C. Pham, *Anal. Bioanal. Chem.*, 2012, **402**, 1813-1826.
31. H. Teymourian, M. Parrilla, J. R. Sempionatto, N. F. Montiel, A. Barfidokht, R. Van Echelpoel, K. De Wael and J. Wang, *ACS Sens.*, 2020, **5**, 2679-2700.
32. J. Rivnay, S. Inal, A. Salleo, R. M. Owens, M. Berggren and G. G. Malliaras, *Nat. Rev. Mater.*, 2018, **3**, 17086.
33. S. H. Kim, K. Hong, W. Xie, K. H. Lee, S. Zhang, T. P. Lodge and C. D. Frisbie, *Adv. Mater.*, 2013, **25**, 1822-1846.
34. G. Cadilha Marques, D. Weller, A. T. Erozan, X. Feng, M. Tahoori and J. Aghassi-Hagmann, *Adv. Mater.*, 2019, **31**, 1806483.
35. H. F. Ling, D. A. Koutsouras, S. Kazemzadeh, Y. van de Burgt,

- F. Yan and P. Gkoupidenis, *Appl. Phys. Rev.*, 2020, **7**, 011307.
36. H. Zhong, Q. C. Sun, G. Li, J. Y. Du, H. Y. Huang, E. J. Guo, M. He, C. Wang, G. Z. Yang, C. Ge and K. J. Jin, *Chin. Phys. B*, 2020, **29**, 040703.
37. T. Fujimoto and K. Awaga, *Phys. Chem. Chem. Phys.*, 2013, **15**, 8983-9006.
38. R. Jalem, M. J. D. Rushton, W. Manalastas, M. Nakayama, T. Kasuga, J. A. Kilner and R. W. Grimes, *Chem. Mater.*, 2015, **27**, 2821-2831.
39. M. Watanabe, M. L. Thomas, S. Zhang, K. Ueno, T. Yasuda and K. Dokko, *Chem. Rev.*, 2017, **117**, 7190-7239.
40. J. M. Lu, F. Yan and J. Texter, *Prog. Polym. Sci.*, 2009, **34**, 431-448.
41. C. Duan, J. Huang, N. Sullivan and R. O'Hayre, *Appl. Phys. Rev.*, 2020, **7**, 011314.
42. K. D. Kreuer, *Annu. Rev. Mater. Res.*, 2003, **33**, 333-359.
43. C. J. Wan, L. Q. Zhu, J. M. Zhou, Y. Shi and Q. Wan, *Nanoscale*, 2014, **6**, 4491-4497.
44. B. Wang, W. Huang, L. Chi, M. Al-Hashimi, T. J. Marks and A. Facchetti, *Chem. Rev.*, 2018, **118**, 5690-5754.
45. M. J. Panzer and C. D. Frisbie, *Adv. Mater.*, 2008, **20**, 3177-3180.
46. S. K. Garlapati, M. Divya, B. Breitung, R. Kruk, H. Hahn and S. Dasgupta, *Adv. Mater.*, 2018, **30**, e1707600.
47. J. Rivnay, P. Leleux, M. Ferro, M. Sessolo, A. Williamson, D. A. Koutsouras, D. Khodagholy, M. Ramuz, X. Strakosas, R. M. Owens, C. Benar, J. M. Badier, C. Bernard and G. G. Malliaras, *Sci. Adv.*, 2015, **1**, e1400251.
48. H. T. Yuan, H. Shimotani, A. Tsukazaki, A. Ohtomo, M. Kawasaki and Y. Iwasa, *J. Am. Chem. Soc.*, 2010, **132**, 6672-6678.
49. F. Buth, D. Kumar, M. Stutzmann and J. A. Garrido, *Appl. Phys. Lett.*, 2011, **98**, 153302.
50. H. K. Li, T. P. Chen, P. Liu, S. G. Hu, Y. Liu, Q. Zhang and P. S. Lee, *J. Appl. Phys.*, 2016, **119**, 244505.
51. L. Suo, O. Borodin, T. Gao, M. Olguin, J. Ho, X. Fan, C. Luo, C. Wang and K. Xu, *Science*, 2015, **350**, 938-943.
52. W. Fu, L. Jiang, E. P. van Geest, L. M. Lima and G. F. Schneider, *Adv. Mater.*, 2017, **29**, 1603610.
53. G. Tarabella, F. M. Mohammadi, N. Coppede, F. Barbero, S. Iannotta, C. Santato and F. Ciccoira, *Chem. Sci.*, 2013, **4**, 1395-1409.
54. K. S. Ngai, S. Ramesh, K. Ramesh and J. C. Juan, *Ionics*, 2016, **22**, 1259-1279.
55. H. M. Yang, Y. K. Kwon, S. B. Lee, S. Kim, K. Hong and K. H. Lee, *ACS Appl. Mater. Interfaces*, 2017, **9**, 8813-8818.
56. F. Zare Bidoky, W. J. Hyun, D. Song and C. D. Frisbie, *Appl. Phys. Lett.*, 2018, **113**, 053301.
57. X. Feng, A. Scholz, M. B. Tahoouri and J. Aghassi-Hagmann, *IEEE Trans. Electron Devices*, 2020, **67**, 4918-4923.
58. J. H. Choi, W. Xie, Y. Gu, C. D. Frisbie and T. P. Lodge, *ACS Appl. Mater. Interfaces*, 2015, **7**, 7294-7302.
59. S. K. Fullerton-Shirey and J. K. Maranas, *Macromolecules*, 2009, **42**, 2142-2156.
60. B. N. Pal, B. M. Dhar, K. C. See and H. E. Katz, *Nat. Mater.*, 2009, **8**, 898-903.
61. R. Ponce Ortiz, A. Facchetti and T. J. Marks, *Chem. Rev.*, 2010, **110**, 205-239.
62. Y. Kutovyi, I. Zadorozhnyi, V. Handziuk, H. Hlukhova, N. Boichuk, M. Petrychuk and S. Vitusevich, *Nano Lett.*, 2018, **18**, 7305-7313.
63. M. Singh, G. Palazzo, G. Romanazzi, G. P. Suranna, N. Ditaranto, C. Di Franco, M. V. Santacroce, M. Y. Mulla, M. Magliulo, K. Manoli and L. Torsi, *Faraday Discuss.*, 2014, **174**, 383-398.
64. Y. Ren, H. Yuan, X. Wu, Z. Chen, Y. Iwasa, Y. Cui, H. Y. Hwang and K. Lai, *Nano Lett.*, 2015, **15**, 4730-4736.
65. L. Mracek, T. Syrový, S. Pretl, S. Nespurek and A. Hamacek, *2016 39th International Spring Seminar on Electronics Technology (Isse)*, 2016, 66-70.
66. F. Leonardi, S. Casalini, Q. Zhang, S. Galindo, D. Gutierrez and M. Mas-Torrent, *Adv. Mater.*, 2016, **28**, 10311-10316.
67. S. Thiemann, M. Gruber, I. Lokteva, J. Hirschmann, M. Halik and J. Zaumseil, *ACS Appl. Mater. Interfaces*, 2013, **5**, 1656-1662.
68. D. Weller, G. C. Marques, J. Aghassi-Hagmann and M. B. Tahoouri, *IEEE Electron Device Lett.*, 2018, **39**, 831-834.
69. R. B. Rashid, R. J. Ciecowski and J. Rivnay, *Flex. Print. Electron.*, 2020, **5**, 014007.
70. A. F. Paterson, A. Savva, S. Wustoni, L. Tsetseris, B. D. Paulsen, H. Faber, A. H. Emwas, X. Chen, G. Nikiforidis, T. C. Hidalgo, M. Moser, I. P. Maria, J. Rivnay, I. McCulloch, T. D. Anthopoulos and S. Inal, *Nat. Commun.*, 2020, **11**, 3004.
71. Y. S. Rim, *J. Inf. Disp.*, 2020, **21**, 203-210.
72. P. Romele, P. Gkoupidenis, D. A. Koutsouras, K. Lieberth, Z. M. Kovacs-Vajna, P. W. M. Blom and F. Torricelli, *Nat. Commun.*, 2020, **11**, 3743.
73. A. Giovannitti, R. B. Rashid, Q. Thiburce, B. D. Paulsen, C. Cendra, K. Thorley, D. Moia, J. T. Mefford, D. Hanifi, W. Y. Du, M. Moser, A. Salleo, J. Nelson, I. McCulloch and J. Rivnay, *Adv. Mater.*, 2020, **32**, 1908047.
74. F. Yu, L. Q. Zhu, H. Xiao, W. T. Gao and Y. B. Guo, *Adv. Funct. Mater.*, 2018, **28**, 1804025.
75. M. Kettner, I. Vladimirov, A. J. Strudwick, M. G. Schwab and R. T. Weitz, *J. Appl. Phys.*, 2015, **118**, 025501.
76. C. B. Nielsen, A. Giovannitti, D. T. Sbircea, E. Bandiello, M. R. Niazi, D. A. Hanifi, M. Sessolo, A. Amassian, G. G. Malliaras, J. Rivnay and I. McCulloch, *J. Am. Chem. Soc.*, 2016, **138**, 10252-10259.
77. A. Giovannitti, K. J. Thorley, C. B. Nielsen, J. Li, M. J. Donahue, G. G. Malliaras, J. Rivnay and I. McCulloch, *Adv. Funct. Mater.*, 2018, **28**, 1706325.
78. S. Inal, G. G. Malliaras and J. Rivnay, *Nat. Commun.*, 2017, **8**, 1767.
79. A. G. Polyravas, V. F. Curto, N. Schaefer, A. B. Calia, A. Guimera-Brunet, J. A. Garrido and G. G. Malliaras, *Flexible Printed Electron.*, 2019, **4**, 044003.
80. V. F. Curto, B. Marchiori, A. Hama, A. M. Pappa, M. P. Ferro, M. Braendlein, J. Rivnay, M. Flocchi, G. G. Malliaras, M. Ramuz and R. M. Owens, *Microsyst. Nanoeng.*, 2017, **3**, 17028.
81. P. Andersson Ersman, R. Lassnig, J. Strandberg, D. Tu, V. Keshmiri, R. Forchheimer, S. Fabiano, G. Gustafsson and M. Berggren, *Nat. Commun.*, 2019, **10**, 5053.
82. W. Lee, D. Kim, N. Matsuhisa, M. Nagase, M. Sekino, G. G. Malliaras, T. Yokota and T. Someya, *Proc. Natl. Acad. Sci. U. S. A.*, 2017, **114**, 10554-10559.
83. M. Hamedi, L. Herlogsson, X. Crispin, R. Marcilla, M. Berggren and O. Inganäs, *Adv. Mater.*, 2009, **21**, 573-577.
84. A. T. Erozan, G. C. Marques, M. S. Golanbari, R. Bishnoi, S. Dehm, J. Aghassi-Hagmann and M. B. Tahoouri, *IEEE Transactions on VLSI Systems*, 2018, **26**, 2935-2946.
85. S. Zhang, P. Kumar, A. S. Nouas, L. Fontaine, H. Tang and F.

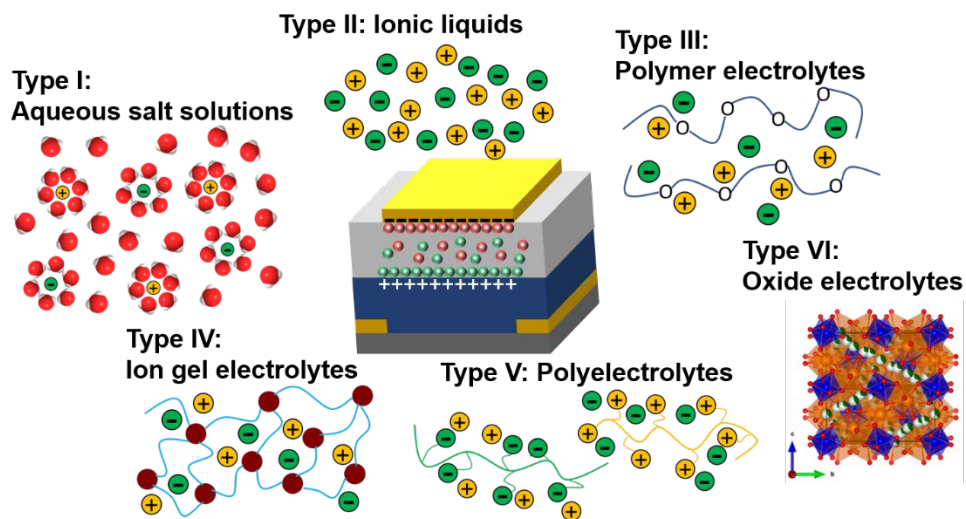
- Cicoira, *APL Mater.*, 2015, **3**, 014911.
86. K. Manoli, P. Seshadri, M. Singh, C. Di Franco, A. Nacci, G. Palazzo and L. Torsi, *Phys. Chem. Chem. Phys.*, 2017, **19**, 20573-20581.
87. P. Bergveld, *IEEE Trans. Biomed. Eng.*, 1970, **17**, 70-71.
88. P. Bergveld and N. F. Derooij, *Sens. Actuators, B*, 1981, **1**, 5-15.
89. M. Krüger, M. R. Buitelaar, T. Nussbaumer, C. Schönenberger and L. Forró, *Appl. Phys. Lett.*, 2001, **78**, 1291-1293.
90. S. Rosenblatt, Y. Yaish, J. Park, J. Gore, V. Sazonova and P. L. McEuen, *Nano Lett.*, 2002, **2**, 869-872.
91. D. A. Koutsouras, G. G. Malliaras and P. Gkoupidenis, *MRS Commun.*, 2018, **8**, 493-497.
92. A. Giovannitti, D. T. Sbircea, S. Inal, C. B. Nielsen, E. Bandiello, D. A. Hanifi, M. Sessolo, G. G. Malliaras, I. McCulloch and J. Rivnay, *Proc. Natl. Acad. Sci. U. S. A.*, 2016, **113**, 12017-12022.
93. M. Moser, T. C. Hidalgo, J. Surgailis, J. Gladisch, S. Ghosh, R. Sheelamanthula, Q. Thiburce, A. Giovannitti, A. Salleo, N. Gasparini, A. Wadsworth, I. Zozoulenko, M. Berggren, E. Stavrinidou, S. Inal and I. McCulloch, *Adv. Mater.*, 2020, **32**, e2002748.
94. A. Savva, R. Hallani, C. Cendra, J. Surgailis, T. C. Hidalgo, S. Wustoni, R. Sheelamanthula, X. Chen, M. Kirkus, A. Giovannitti, A. Salleo, I. McCulloch and S. Inal, *Adv. Funct. Mater.*, 2020, **30**, 1907657.
95. L. Q. Flagg, R. Giridharagopal, J. J. Guo and D. S. Ginger, *Chem. Mater.*, 2018, **30**, 5380-5389.
96. L. Q. Flagg, C. G. Bischak, J. W. Onorato, R. B. Rashid, C. K. Luscombe and D. S. Ginger, *J. Am. Chem. Soc.*, 2019, **141**, 4345-4354.
97. L. Q. Flagg, C. G. Bischak, R. J. Quezada, J. W. Onorato, C. K. Luscombe and D. S. Ginger, *ACS Mater. Lett.*, 2020, **2**, 254-260.
98. A. Savva, C. Cendra, A. Giugni, B. Torre, J. Surgailis, D. Ohayon, A. Giovannitti, I. McCulloch, E. Di Fabrizio, A. Salleo, J. Rivnay and S. Inal, *Chem. Mater.*, 2019, **31**, 927-937.
99. C. Cendra, A. Giovannitti, A. Savva, V. Venkatraman, I. McCulloch, A. Salleo, S. Inal and J. Rivnay, *Adv. Funct. Mater.*, 2019, **29**, 1807034.
100. A. Melianas, T. J. Quill, G. LeCroy, Y. Tuchman, H. V. Loo, S. T. Keene, A. Giovannitti, H. R. Lee, I. P. Maria, I. McCulloch and A. Salleo, *Sci. Adv.*, 2020, **6**, eabb2958.
101. Y. van de Burgt, E. Lubberman, E. J. Fuller, S. T. Keene, G. C. Faria, S. Agarwal, M. J. Marinella, A. Alec Talin and A. Salleo, *Nat. Mater.*, 2017, **16**, 414-418.
102. S. Park, S. W. Heo, W. Lee, D. Inoue, Z. Jiang, K. Yu, H. Jinno, D. Hashizume, M. Sekino, T. Yokota, K. Fukuda, K. Tajima and T. Someya, *Nature*, 2018, **561**, 516-521.
103. W. Lee, S. Kobayashi, M. Nagase, Y. Jimbo, I. Saito, Y. Inoue, T. Yambe, M. Sekino, G. G. Malliaras, T. Yokota, M. Tanaka and T. Someya, *Sci. Adv.*, 2018, **4**, eaau2426.
104. Q. Liu, Y. Liu, F. Wu, X. Cao, Z. Li, M. Alharbi, A. N. Abbas, M. R. Amer and C. Zhou, *ACS Nano*, 2018, **12**, 1170-1178.
105. Y. S. Rim, S. H. Bae, H. Chen, J. L. Yang, J. Kim, A. M. Andrews, P. S. Weiss, Y. Yang and H. R. Tseng, *ACS Nano*, 2015, **9**, 12174-12181.
106. P. Yang, G. S. Cai, X. Z. Wang and Y. L. Pei, *IEEE Trans. Electron Devices*, 2019, **66**, 3554-3559.
107. D. Ohayon, G. Nikiiforidis, A. Savva, A. Giugni, S. Wustoni, T. Palanisamy, X. Chen, I. P. Maria, E. Di Fabrizio, P. Costa, I. McCulloch and S. Inal, *Nat. Mater.*, 2020, **19**, 456-463.
108. P. Gkoupidenis, D. A. Koutsouras and G. G. Malliaras, *Nat. Commun.*, 2017, **8**, 15448.
109. N. Nakatsuka, K. A. Yang, J. M. Abendroth, K. M. Cheung, X. Xu, H. Yang, C. Zhao, B. Zhu, Y. S. Rim, Y. Yang, P. S. Weiss, M. N. Stojanovic and A. M. Andrews, *Science*, 2018, **362**, 319-324.
110. R. Faddoul, R. Coppard and T. Berthelot, presented in part at the 2014 IEEE Sensors, 2014.
111. J. Kim, Y. S. Rim, H. Chen, H. H. Cao, N. Nakatsuka, H. L. Hinton, C. Zhao, A. M. Andrews, Y. Yang and P. S. Weiss, *ACS Nano*, 2015, **9**, 4572-4582.
112. M. Magliulo, A. Mallardi, M. Y. Mulla, S. Cotrone, B. R. Pistillo, P. Favia, I. Vikholm-Lundin, G. Palazzo and L. Torsi, *Adv. Mater.*, 2013, **25**, 2090-2094.
113. J. Janata, *ECS Solid State Lett.*, 2012, **1**, M29-M31.
114. S. Ono, K. Miwa, S. Seki and J. Takeya, *Appl. Phys. Lett.*, 2009, **94**, 063301.
115. D. Okaue, I. Tanabe, S. Ono, K. Sakamoto, T. Sato, A. Imanishi, Y. Morikawa, J. Takeya and K. Fukui, *J. Phys. Chem. C*, 2020, **124**, 2543-2552.
116. W. Lu, A. G. Fadeev, B. Qi, E. Smela, B. R. Mattes, J. Ding, G. M. Spinks, J. Mazurkiewicz, D. Zhou, G. G. Wallace, D. R. MacFarlane, S. A. Forsyth and M. Forsyth, *Science*, 2002, **297**, 983-987.
117. R. Misra, M. McCarthy and A. F. Hebard, *Appl. Phys. Lett.*, 2007, **90**, 052905.
118. S. Ono, S. Seki, R. Hirahara, Y. Tominari and J. Takeya, *Appl. Phys. Lett.*, 2008, **92**, 103313.
119. M. H. Yoon, C. Kim, A. Facchetti and T. J. Marks, *J. Am. Chem. Soc.*, 2006, **128**, 12851-12869.
120. M. Kettner, M. Zhou, J. Brill, P. W. M. Blom and R. T. Weitz, *ACS Appl. Mater. Interfaces*, 2018, **10**, 35449-35454.
121. J. Kim, J. Jang, K. Kim, H. Kim, S. H. Kim and C. E. Park, *Adv. Mater.*, 2014, **26**, 7241-7246.
122. C. Jiang, H. B. Ma, D. G. Hasko, X. J. Guo and A. Nathan, *Adv. Electron. Mater.*, 2017, **3**, 1700029.
123. S. Park, S. H. Kim, H. H. Choi, B. Kang and K. Cho, *Adv. Funct. Mater.*, 2020, **30**, 1904590.
124. Q. Zhang, T. S. Kale, E. Plunkett, W. Shi, B. J. Kirby, D. H. Reich and H. E. Katz, *Macromolecules*, 2018, **51**, 6011-6020.
125. J. Lenz, F. del Giudice, F. R. Geisenhof, F. Winterer and R. T. Weitz, *Nat. Nanotechnol.*, 2019, **14**, 579-585.
126. C. Lu, W. Y. Lee, C. C. Shih, M. Y. Wen and W. C. Chen, *ACS Appl. Mater. Interfaces*, 2017, **9**, 25522-25532.
127. J. Choi, J. Kang, C. Lee, K. Jeong and S. G. Im, *Adv. Electron. Mater.*, 2020, **6**, 2000314.
128. E. Stucchi, G. Dell'Erba, P. Colpani, Y. H. Kim and M. Caironi, *Adv. Electron. Mater.*, 2018, **4**, 1800340.
129. D. Ji, T. Li, Y. Zou, M. Chu, K. Zhou, J. Liu, G. Tian, Z. Zhang, X. Zhang, L. Li, D. Wu, H. Dong, Q. Miao, H. Fuchs and W. Hu, *Nat. Commun.*, 2018, **9**, 2339.
130. B. W. Yao, J. Li, X. D. Chen, M. X. Yu, Z. C. Zhang, Y. Li, T. B. Lu and J. Zhang, *Advanced Functional Materials*, 2021, DOI: 10.1002/adfm.202100069, 2100069.
131. C. Samanta, R. R. Ghimire and B. Ghosh, *IEEE Trans. Electron Devices*, 2018, **65**, 2827-2832.
132. Y. Zhu, G. Liu, Z. Xin, C. Fu, Q. Wan and F. Shan, *ACS Appl. Mater. Interfaces*, 2020, **12**, 1061-1068.
133. H. Shimotani, H. Suzuki, K. Ueno, M. Kawasaki and Y. Iwasa,

- Appl. Phys. Lett.*, 2008, **92**, 242107.
134. S. K. Garlapati, N. Mishra, S. Dehm, R. Hahn, R. Kruk, H. Hahn and S. Dasgupta, *ACS Appl. Mater. Interfaces*, 2013, **5**, 11498-11502.
135. S. A. Singaraju, T. T. Baby, F. Neuper, R. Kruk, J. A. Hagmann, H. Hahn and B. Breitung, *ACS Appl. Electron. Mater.*, 2019, **1**, 1538-1544.
136. T. T. Baby, S. K. Garlapati, S. Dehm, M. Haming, R. Kruk, H. Hahn and S. Dasgupta, *ACS Nano*, 2015, **9**, 3075-3083.
137. P. Grey, L. Pereira, S. Pereira, P. Barquinha, I. Cunha, R. Martins and E. Fortunato, *Adv. Electron. Mater.*, 2016, **2**, 1500414.
138. B. K. Sharma, A. Stoesser, S. K. Mondal, S. K. Garlapati, M. H. Fawey, V. S. K. Chakravadhanula, R. Kruk, H. Hahn and S. Dasgupta, *ACS Appl. Mater. Interfaces*, 2018, **10**, 22408-22418.
139. C. G. Lu, Q. Fu, S. M. Huang and J. Liu, *Nano Lett.*, 2004, **4**, 623-627.
140. G. P. Siddons, D. Merchin, J. H. Back, J. K. Jeong and M. Shim, *Nano Lett.*, 2004, **4**, 927-931.
141. S. Chao and M. S. Wrighton, *J. Am. Chem. Soc.*, 1987, **109**, 2197-2199.
142. S. Chao and M. S. Wrighton, *J. Am. Chem. Soc.*, 1987, **109**, 6627-6631.
143. S. K. Garlapati, J. S. Gebauer, S. Dehm, M. Bruns, M. Winterer, H. Hahn and S. Dasgupta, *Adv. Electron. Mater.*, 2017, **3**, 1600476.
144. S. Dasgupta, G. Stoesser, N. Schweikert, R. Hahn, S. Dehm, R. Kruk and H. Hahn, *Adv. Funct. Mater.*, 2012, **22**, 4909-4919.
145. X. Y. Tao, V. Koncar and C. Dufour, *J. Electrochem. Soc.*, 2011, **158**, H572-H577.
146. A. Stoesser, F. von Seggern, S. Purohit, B. Nasr, R. Kruk, S. Dehm, W. Di, H. Hahn and S. Dasgupta, *Nanotechnology*, 2016, **27**, 415205.
147. B. Nasr, D. Wang, R. Kruk, H. Rosner, H. Hahn and S. Dasgupta, *Adv. Funct. Mater.*, 2013, **23**, 1750-1758.
148. G. C. Marques, S. K. Garlapati, D. Chatterjee, S. Dehm, S. Dasgupta, J. Aghassi and M. B. Tahoori, *IEEE Trans. Electron Devices*, 2017, **64**, 279-285.
149. D. Zhao, Y. Zhu, W. Cheng, W. Chen, Y. Wu and H. Yu, *Adv. Mater.*, 2020, DOI: 10.1002/adma.202000619, e2000619.
150. G. C. Marques, A. Birla, A. Arnal, S. Dehm, E. Ramon, M. B. Tahoori and J. Aghassi-Hagmann, *IEEE Trans. Electron Devices*, 2020, **67**, 3146-3151.
151. Y. He, P. G. Boswell, P. Buhlmann and T. P. Lodge, *J. Phys. Chem. B*, 2007, **111**, 4645-4652.
152. J. H. Cho, J. Lee, Y. He, B. Kim, T. P. Lodge and C. D. Frisbie, *Adv. Mater.*, 2008, **20**, 686-690.
153. K. Hong, Y. H. Kim, S. H. Kim, W. Xie, W. D. Xu, C. H. Kim and C. D. Frisbie, *Adv. Mater.*, 2014, **26**, 7032-7037.
154. J. H. Cho, J. Lee, Y. Xia, B. Kim, Y. He, M. J. Renn, T. P. Lodge and C. D. Frisbie, *Nat. Mater.*, 2008, **7**, 900-906.
155. Y. Lee, J. Y. Oh, W. Xu, O. Kim, T. R. Kim, J. Kang, Y. Kim, D. Son, J. B. Tok, M. J. Park, Z. Bao and T. W. Lee, *Sci. Adv.*, 2018, **4**, eaat7387.
156. S. P. White, K. D. Dorfman and C. D. Frisbie, *J. Phys. Chem. C*, 2016, **120**, 108-117.
157. Y. Xia, W. Zhang, M. J. Ha, J. H. Cho, M. J. Renn, C. H. Kim and C. D. Frisbie, *Adv. Funct. Mater.*, 2010, **20**, 587-594.
158. W. J. Hyun, L. E. Chaney, J. R. Downing, A. C. M. de Moraes and M. C. Hersam, *Faraday Discuss.*, 2021, DOI: 10.1039/c9fd00113a, DOI: 10.1039/C1039FD00113A.
159. B. Nketia - Yawson, G. D. Tabi, J. W. Jo and Y. Y. Noh, *Adv. Mater. Interfaces*, 2020, **7**, 2000842.
160. K. G. Cho, H. J. Kim, H. M. Yang, K. H. Seol, S. J. Lee and K. H. Lee, *ACS Appl. Mater. Interfaces*, 2018, **10**, 40672-40680.
161. B. Nketia-Yawson, S. J. Kang, G. D. Tabi, A. Perinot, M. Caironi, A. Facchetti and Y. Y. Noh, *Adv. Mater.*, 2017, **29**, 1605685.
162. B. Nketia-Yawson, G. D. Tabi and Y. Y. Noh, *ACS Appl. Mater. Interfaces*, 2019, **11**, 17610-17616.
163. H. J. Lee, S. Lee, Y. Ji, K. G. Cho, K. S. Choi, C. Jeon, K. H. Lee and K. Hong, *ACS Appl. Mater. Interfaces*, 2019, **11**, 40243-40251.
164. Y. Ji, H. J. Lee, S. Lee, K. G. Cho, K. H. Lee and K. Hong, *Adv. Mater. Interfaces*, 2019, **6**, 1900883.
165. J. Sun, S. Oh, Y. Choi, S. Seo, M. J. Oh, M. Lee, W. B. Lee, P. J. Yoo, J. H. Cho and J. H. Park, *Adv. Funct. Mater.*, 2018, **28**, 1804397.
166. J. H. Choi, Y. Gu, K. Hong, W. Xie, C. D. Frisbie and T. P. Lodge, *ACS Appl. Mater. Interfaces*, 2014, **6**, 19275-19281.
167. W. Zhang, Q. Zhao and J. Yuan, *Angew. Chem. Int. Ed. Engl.*, 2018, **57**, 6754-6773.
168. H. J. Kim, B. Chen, Z. Suo and R. C. Hayward, *Science*, 2020, **367**, 773-776.
169. H. Sinno, S. Fabiano, X. Crispin, M. Berggren and I. Engquist, *Appl. Phys. Lett.*, 2013, **102**, 113306.
170. L. L. Du, D. D. He, Y. X. Liu, M. S. Xu, Q. P. Wang, Q. Xin and A. M. Song, *IEEE Electron Device Lett.*, 2018, **39**, 1334-1337.
171. L. Herlogsson, X. Crispin, S. Tierney and M. Berggren, *Adv. Mater.*, 2011, **23**, 4684-4689.
172. D. Zhao, S. Fabiano, M. Berggren and X. Crispin, *Nat. Commun.*, 2017, **8**, 14214.
173. Y. H. Liu, L. Q. Zhu, P. Feng, Y. Shi and Q. Wan, *Adv. Mater.*, 2015, **27**, 5599-5604.
174. S. Fabiano, S. Braun, M. Fahlman, X. Crispin and M. Berggren, *Adv. Funct. Mater.*, 2014, **24**, 695-700.
175. N. Liu, L. Gan, Y. Liu, W. J. Gui, W. Li and X. H. Zhang, *Appl. Surf. Sci.*, 2017, **419**, 206-212.
176. G. D. Wu, J. Zhang, X. Wan, Y. Yang and S. H. Jiang, *J. Mater. Chem. C*, 2014, **2**, 6249-6255.
177. I. Cunha, R. Barras, P. Grey, D. Gaspar, E. Fortunato, R. Martins and L. Pereira, *Adv. Funct. Mater.*, 2017, **27**, 1606755.
178. P. Grey, S. N. Fernandes, D. Gaspar, E. Fortunato, R. Martins, M. H. Godinho and L. Pereira, *Adv. Funct. Mater.*, 2018, **29**, 1805279.
179. S. Dai, Y. Chu, D. Liu, F. Cao, X. Wu, J. Zhou, B. Zhou, Y. Chen and J. Huang, *Nat. Commun.*, 2018, **9**, 2737.
180. W. Qian, J. Texter and F. Yan, *Chem. Soc. Rev.*, 2017, **46**, 1124-1159.
181. A. Laiho, L. Herlogsson, R. Forchheimer, X. Crispin and M. Berggren, *Proc. Natl. Acad. Sci. U. S. A.*, 2011, **108**, 15069-15073.
182. L. Herlogsson, X. Crispin, N. D. Robinson, M. Sandberg, O. J. Hagel, G. Gustafsson and M. Berggren, *Adv. Mater.*, 2007, **19**, 97-101.
183. G. Wu, P. Feng, X. Wan, L. Zhu, Y. Shi and Q. Wan, *Sci. Rep.*, 2016, **6**, 23578.
184. L. Q. Guo, J. Tao, L. Q. Zhu, H. Xiao, W. T. Gao, F. Yu and Y. M. Fu, *Org. Electron.*, 2018, **61**, 312-317.
185. Y. H. Liu, X. Wan, L. Q. Zhu, Y. Shi and Q. Wan, *IEEE Electron*

- Device Lett.*, 2014, **35**, 1257-1259.
186. M. Galliani, C. Diacci, M. Berto, M. Sensi, V. Beni, M. Berggren, M. Borsari, D. T. Simon, F. Biscarini and C. A. Bortolotti, *Adv. Mater. Interfaces*, 2020, **7**, 2001218.
187. J. M. Zhou, Y. H. Liu, Y. Shi and Q. Wan, *IEEE Electron Device Lett.*, 2014, **35**, 280-282.
188. K. Banger, C. Warwick, J. Lang, K. Broch, J. E. Halpert, J. Socratous, A. Brown, T. Leedham and H. Sirringhaus, *Chem. Sci.*, 2016, **7**, 6337-6346.
189. X. Zhuang, S. Patel, C. Zhang, B. Wang, Y. Chen, H. Liu, V. P. Dravid, J. Yu, Y. Y. Hu, W. Huang, A. Facchetti and T. J. Marks, *J. Am. Chem. Soc.*, 2020, **142**, 12440-12452.
190. B. Zhang, Y. Liu, S. Agarwala, M. L. Yeh and H. E. Katz, *ACS Appl. Mater. Interfaces*, 2011, **3**, 4254-4261.
191. E. J. Fuller, F. E. Gabaly, F. Leonard, S. Agarwal, S. J. Plimpton, R. B. Jacobs-Gedrim, C. D. James, M. J. Marinella and A. A. Talin, *Adv. Mater.*, 2017, **29**, 1604310.
192. X. C. Liang, Z. W. Li, L. Liu, S. J. Chen, X. Z. Wang and Y. L. Pei, *Appl. Phys. Lett.*, 2020, **116**, 012102.
193. L. Q. Zhu, C. J. Wan, L. Q. Guo, Y. Shi and Q. Wan, *Nat. Commun.*, 2014, **5**, 3158.
194. R. D. Nikam, M. Kwak, J. Lee, K. G. Rajput, W. Banerjee and H. Hwang, *Sci. Rep.*, 2019, **9**, 18883.
195. V. Lacivita, N. Artrith and G. Ceder, *Chem. Mater.*, 2018, **30**, 7077-7090.
196. J. Li, D. Jiang, Y. Yang, Y. Zhou, Q. Chen and J. Zhang, *Adv. Electron. Mater.*, 2020, **6**, 1901363.
197. F. Neuper, G. C. Marques, S. A. Singaraju, R. Kruk, J. Aghassi-Hagmann, H. Hahn and B. Breitung, *IEEE Trans. Electron Devices*, 2020, **67**, 3828-3833.
198. Z. Y. Ren, L. Q. Zhu, Y. B. Guo, T. Y. Long, F. Yu, H. Xiao and H. L. Lu, *ACS Appl. Mater. Interfaces*, 2020, **12**, 7833-7839.
199. X. Wan, Y. Yang, P. Feng, Y. Shi and Q. Wan, *IEEE Electron Device Lett.*, 2016, **37**, 299-302.
200. E. Bandiello, M. Sessolo and H. J. Bolink, *J. Mater. Chem. C*, 2014, **2**, 10277-10281.
201. K. Schmoltner, J. Kofler, A. Klug and E. J. List-Kratochvil, *Adv. Mater.*, 2013, **25**, 6895-6899.
202. M. Sessolo, J. Rivnay, E. Bandiello, G. G. Malliaras and H. J. Bolink, *Adv. Mater.*, 2014, **26**, 4803-4807.
203. C. G. Bischak, L. Q. Flagg and D. S. Ginger, *Adv. Mater.*, 2020, **32**, 2002610.
204. K. H. Lee, S. Zhang, Y. Gu, T. P. Lodge and C. D. Frisbie, *ACS Appl. Mater. Interfaces*, 2013, **5**, 9522-9527.
205. L. Huang, Z. Wang, J. Chen, B. Wang, Y. Chen, W. Huang, L. Chi, T. J. Marks and A. Facchetti, *Adv. Mater.*, 2021, DOI: 10.1002/adma.202007041, e2007041.

Review

Table of content:

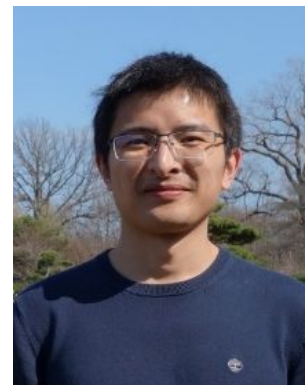


In this review, recent progress in different types of electrolyte dielectric materials for electrolyte gated transistors (EGTs) are summarized, along with the structures and operation of EGTs and their relevant applications.

Review

Photograph and biography of authors

Wei Huang obtained his B.S. (2010) in physics from Nankai University and his Ph.D. (2016) in optical engineering from University of Electronic Science and Technology of China (UESTC). He was a postdoctoral fellow and later a Research Assistant Professor in the Department of Chemistry, Northwestern University, under the supervision of Professor Tobin J. Marks and Professor Antonio Facchetti. Currently, he is a Research Professor in School of Automation Engineering, UESTC. His research interests include flexible/stretchable electronics, transistor-based multifunctional sensors and solar cells.



Tobin Marks is Ipatieff Professor of Catalysis and Materials Science and Engineering at Northwestern U. He holds a B.S. from the U. of Maryland and a Ph.D. from MIT. Recognitions: U.S. National Medal of Science, ACS Priestley Medal, Spanish Asturias Prize, MRS Von Hippel Award, Dreyfus Prize in Chemical Sciences, NAS Award in Chemical Sciences, CAS President's International Distinguished Scientist Award, Israel Harvey Prize. Membership: U.S., European, German, Italian, and Indian Academies of Science, U.S. NAE and NAI, American Academy of Arts and Sciences; RSC, MRS, ACS, AIC Fellow. Research interests: unconventional catalysis, soft and hard matter electronic materials, and photovoltaics.



Antonio Facchetti obtained his Ph.D. in Chemical Sciences from the University of Milan. He is a co-founder and currently the Chief Technology Officer of Flexterra Corporation and an Adjunct Professor of Chemistry at Northwestern University. Dr. Facchetti has published more than 500 research articles, 14 book chapters, and holds more than 120 patents (H-index 107). He is a Fellow of the Kavli Foundation, AAAS, MRS, ACS PMSE, RSC, and the National Academy of Inventors. He received the Italian Chemical Society Research Prize, the 2016 ACS Award for Creative Invention and the Giulio Natta Gold Medal.

